UNIVERSIDADE DE LISBOA
FACULDADE DE CIÊNCIAS
DEPARTAMENTO DE FÍSICA

Cosmological propagation of astrophysical gravitational waves

Chi Tou Iu

Mestrado em Física
Especialização em Astrofísica e Cosmologia

Dissertação orientada por:
Professor Nelson Nunes
Professor António Silva

2023

Acknowledgments

First, I would like to thank my supervisors, Professor Nelson Nunes and Professor António Silva for guiding me in this dissertation throughout the year, assist me to set up the framework, and give me valuable suggestions on my work. I am extremely grateful for the effort they have made for me, and inspired by their passion and dedication to astronomy.

Next, I would like to thank Professor Maria Margarida Cruz for giving me the chance to study at FCUL and other Professors that gave me inspirations on physics and supports, like Mykola Tasinkevych, José Figueiredo, Ismael Tereno and others. These supports drove me through the tough time during the transition from the field of Electronic Engineering to Physics.

Also, a thanks to my classmates who have given me encouragement during the adventure on this master's degree, José Ferreira, Duarte Almeida, Miguel Pinto, Pedro Garcia and others.

Lastly, I must give my thanks to my family, who provide me an opportunity to pursue my interest, and financial supports which make the stay in Portugal possible, and giving me strength as always. I really enjoy Physics and hopefully I can go further in the coming future.

Resumo

Nesta dissertação, fazemos previsões de constrangimentos para dois modelos de Gravidade Teleparalela Simétrica usando a abordagem da Matriz de Fisher. Para estudar estes modelos usamos dados das Supernovas Ia para primeiro nos fornecer a abundância de matéria hoje e construímos catálogos de sirenes padrão com base nas especificações de três observatórios de ondas gravitacionais: LIGO, ET e LISA. O objectivo consiste em prever as suas respectivas capacidades em restringir os parâmetros dos modelos e consequentemente de averiguar se seremos capazes de distingui-los do modelo padrão da cosmologia ΛCDM.

O modelo ΛCDM é bem conhecido por ser o modelo mais simples que fornece uma boa descrição das propriedades do Universo, tal como a existência e a estrutura da radiação cósmica de fundo nos micro-ondas (CMB), que é a evidência direta da expansão do Universo; a expansão acelerada do universo descoberta a partir do brilho e desvio para o vermelho de supernovas distantes; e a homogeneidade e isotropia em escalas suficientemente grandes do nosso Universo. Apesar do sucesso do modelo ΛCDM, ele ainda enfrenta algumas inconsistências, tal como a tensão de Hubble (o valor obtido a partir de dados de supernovas é significativamente maior do que o inferido usando a escala angular das flutuações da radiação cósmica de fundo) e as anomalias nas anisotropias do CMB (uma polarização ligeiramente rodada na radiação cósmica de fundo que não é explicada pelo modelo padrão).

Durante décadas, os cientistas tentaram propor um modelo alternativo para resolver estas dificuldades modificando a ação de Einstein-Hilbert, onde em vez de se usar a curvatura para descrever a gravidade, consideraram-se grandezas matemáticas tais como não-metricidade ou torção. Esta dissertação baseia-se na não-metricidade, que é uma medida da variação do comprimento de um vetor durante o transporte paralelo.

Em 2015, a deteção de ondas gravitacionais abriu uma nova porta para obtermos informações sobre o Universo. Uma das previsões da teoria da Relatividade Geral é que a fusão de sistemas binários como buracos negros ou estrelas de neutrões, resulta numa perda de energia na forma de ondas gravitacionais. Em particular, uma sirene padrão, é um evento que emite ondas eletromagnéticas e ondas gravitacionais, na sequência da fusão, por exemplo, de duas estrelas de neutrões. Um evento deste género fornece-nos a relação direta entre o desvio para o vermelho e distância luminosa ao binário. Esta é uma vantagem enorme em relação aos métodos tradicionais de medição de distâncias pelo método de escada de distâncias cosmológicas, que são susceptíveis a erros de calibração. Infelizmente, até ao momento apenas um evento sirene padrão foi confirmado, GW170817. Isto quer dizer que de momento ainda não somos capazes de colocar constrangimentos aos modelos cosmológicos mas podemos tentar antecipar o nível

de precisão desses constrangimentos no futuro. Para fazer essa análise, geramos catálogos de sirenes padrão realistas e usamos o método da Matriz de Fisher (FM) para fazer a inferência estatística dos modelos em estudo.

O método FM fornece um aumento extraordinário na velocidade de computação em relação aos métodos tradicioanais (de grelha ou Markov Chain Monte Carlo) quando lidamos com modelos com alguns parâmetros. Em vez de computação por força bruta, FM é uma aproximação analítica de uma função de verossimilhança Gaussiana, dado que a probabilidade máxima é conhecida a partir de informação obtida por observações independentes, como as restrições de parâmetros fornecidas pelos dados de supernovas na nossa dissertação.

No primeiro capítulo desta dissertação, apresentamos uma breve história da cosmologia moderna a partir do aparecimento da Relatividade Geral. Em seguida, mencionamos algumas das descobertas mais importantes do último século, tais como a descoberta da radiação cósmica de fundo que indica que o Universo é globalmente plano, velocidade excessiva das galáxias que levou à ideia da matéria escura e a descoberta da expansão acelerada do Universo, que desvendou a existência de uma energia escura. Em seguida, apresentamos os pressupostos estabelecidos pelo modelo ΛCDM e os desafios que este enfrenta. Além disso, explicamos a distância luminosa e apontamos as Sirenes Padrão como ferramentas para a medição de distâncias em cosmologia.

No segundo capítulo, apresentamos as ferramentas matemáticas utilizadas na Relatividade Geral e revemos dois conceitos geométricos chamados torção e não-metricidade que recuperam a formulação padrão da GR sem se usar curvatura. Em seguida, identificamos as fontes do tensor Energia-Momento na equação de campo de Einstein e explicamos a métrica FLRW assumindo o universo homogéneo, isotrópico e plano. Em seguida, mostramos os detalhes da modificação da equação de campo de Einstein com base na não-metricidade. O final deste capítulo explica o comportamento das ondas gravitacionais na gauge transversa e sem traço e como se obtém a distância luminosa das ondas gravitacionais para as teorias $f(Q)$. O resultado é semelhante ao da contraparte electromagnetic (EM) mas com um termo multiplicativo adicional.

No terceiro capítulo, apresentamos a metodologia para calcular a função de verossimilhança dos parâmetros de um modelo usando dados de supernovas e eventos de sirene padrão. Em seguida, explicamos o método Matriz de Fisher e como ele transforma um teste qui-quadrado dependente de dados numa formulação de Matriz de Fisher independente de dados. Depois, mostramos algumas propriedades essenciais da FM, como a transformação de variáveis, maximização e marginalização da função de verossimilhança. Também mostramos o procedimento de implementação de um código para o método da grelha e para o método Fisher Matrix. No final, este capítulo fornece a especificação dos detalhes de dois observatórios de ondas gravitacionais atualmente em operação, Laser Interferometer Gravitational-Wave Observatory (LIGO)-Virgo e dos dois futuros observatórios Laser Interferometer Space Antenna (LISA), e Einstein Telescope (ET). Esses detalhes consistem nas distribuições populacionais esperadas de eventos SS, as incertezas de observação em termos de desvio para o vermelho e o procedimento para a geração de catálogos de SS.

No quarto capítulo, mostramos os principais resultados desta análise aos modelos de $f(Q)$. Demonstramos e comparamos os constrangimentos de parâmetros de diferentes combinações de

missões conjuntas. Devido ao rápido aumento da incerteza com o redshift, os dados do LIGO são incapazes de fornecer qualquer constrangimentos aos modelos por si só. Portanto, LIGO é usado como um complemento para outras missões, tirando partido da boa qualidade em eventos de redshift extremamente baixos que não estão disponíveis com os outros observatórios. Enquanto isso, para o LISA, classificamos três conjuntos de catálogos, o pior, o mediano e o melhor catálogo com base em quão bons são os resultados nos constrangimentos aos parâmetros. Por fim, concluímos que o caso dos dados ET+Pantheon, é o caso que nos oferece os melhores constrangimentos. Isso deve-se ao grande número de eventos SS que se espera que sejam observados pelo Einstein Telescope e com altas precisões de observação. Para o modelo quadrático, ao contrário do primeiro modelo, descobrimos que as restrições de ET+Pantheon não são capazes de superar LISA+Pantheon em todos os parâmetros, e chegamos à conclusão de que a análise conjunta de LISA(pior)+ET+Pantheon é suficiente para constranger o modelo.

No quinto capítulo, estendemos a matriz de Fisher com termos de ordem mais elevados que nos fornecem um método alternativo para aproximar uma probabilidade não-gaussiana com pelo menos 20 vezes maior velocidade computacional do que o método da grelha. Nós fornecemos o procedimento de implementação do código, e escolhemos dois modelos de Quintessência para demostrar que o método DALI dá constrangimentos adequadas nos casos para os quais o método da matriz de Fisher falha.

No último capítulo, damos uma conclusão sobre os principais resultados dos dois modelos de $f(Q)$ e listamos alguns trabalhos futuros que vale a pena explorar.

Palavras-chave: Gravidade Modificada, Matriz de Fisher, Cosmologia Observacional, Sirenes Padrão, Ondas Gravitacionais

Abstract

In this dissertation, we forecast constraints for two types of Symmetric Teleparallel Gravity models using the Fisher Matrix approach. The first features a ΛCDM background with one additional free parameter, where the differences arise at the perturbative level. The second model generalizes the first model with a general power-law term. We first introduce the main concepts of General Relativity and the $f(Q)$ gravity theory. Then, we present the parameter constraints computation methodology. We use grid and Fisher Matrix methods, the former with supernova data and the latter with Gravitational Wave (GW) Luminosity distance mock catalogs. Next, we introduce the specifications and the method of generating mock catalogs for three GW observatories: LIGO-Virgo, LISA, and Einstein Telescope (ET).

We forecast parameter constraints for both $f(Q)$ models with different combinations of mission datasets. We conclude that, for the first model, the ET+Pantheon data provides the best constraints due to the large number of expected GW events, that will be observed with high precision, by the ET at low redshift. For the polynomial model, we find that ET+Pantheon constraints do not outperform LISA+Pantheon on all parameters, so we decided to join the LISA and ET+Pantheon catalogs.

For LISA we used three quality catalog classes (worst, median, and best). The results show that constraints from LISA+ET+Pantheon are similar, regardless of the quality of LISA data, and are the strongest. So, the worst quality LISA catalogs are already good enough to provide the best constraints on the models.

We also extend the Fisher matrix approach with higher order terms, which provide an alternative approximation, especially for non-gaussian likelihoods. We chose two Quintessence models to verify this technique and provide the code implementation procedure. We show that this method gives proper constraints with at least 20 times higher computational speed compared to the grid methods.

Keywords: Modified Gravity, Fisher Information Matrix, Observational Cosmology, Standard Sirens, Gravitational Waves

Contents

List of Tables

List of Figures

Acronyms

ΛCDM Λ Cold Dark Matter xi, 2, 3, 5, 12–14, 29, 34, 36–40, 43, 51

CMB cosmic microwave background 2

DALI Derivative Approximation for Likelihoods xi, 5, 6, 45–50, 52

EFE Einstein Field Equations 10, 14

EM electromagnetic iv, 4

EoS equation of state 10

ET Einstein Telescope iv, x, xi, 18, 29, 32, 36–38, 40–44, 47, 51, 52

FLRW Friedmann-Lemaître-Robertson-Walker 2, 11, 13

FM Fisher Matrix x, xi, 5, 36–40, 42, 43, 47

GR General Relativity 1, 8, 14, 16

GW gravitational wave 4, 5, 15–17, 20, 33, 34, 36, 40, 41, 47

LIGO Laser Interferometer Gravitational-Wave Observatory iv, v, x, xi, 4, 18, 29, 30, 38–43, 51, 52

LISA Laser Interferometer Space Antenna iv, x, xi, 18, 29, 31, 35–44, 51, 52

MBHB massive black hole binary ix, 30

MCMC Markov Chain Monte Carlo 6, 28, 33, 36, 37, 48, 52

PDF probability distribution function 24

SnIa type Ia supernova 4, 18, 35–37, 40

SS standard siren xi, 5, 6, 20, 29–34, 36, 37, 40, 41, 43, 48

STG Symmetric Teleparallel Gravity 12

TT Transverse Traceless 15

Chapter 1

Introduction

In this chapter, we give a brief introduction on the start of modern cosmology and how scientist utilize current observational data to test different universe models which are used to describe our universe, and also the motivation of my work in this dissertation.

1.1 The start of Modern Cosmology

Astronomy is one of the oldest science branches of Physics that human beings have always been interested in, from the observations of stars/constellations for orientation during the navigation era. In modern days, Astrophysics plays a central role in shaping our understanding of the universe through scientific observations and experiments, and Physical cosmology deals with the study of the physical origins and evolution of the universe on large scales through both mathematics and observations.

In the 17th century, Isaac Newton stated in his publication *Principia Mathematica*, the law of universal gravitation, it provided a physical mechanism for Kepler's laws caused by gravitational interaction between the planets and the Sun. General Relativity, a theory of gravitation developed by Albert Einstein between 1907 and 1915, revolutionized and shaped modern thinking of gravitation. It explains that gravitational effects are due to the warping of spacetime between masses. General Relativity (GR) explains the anomalies in the orbits of Mercury which Newtonian mechanics can not. It also predicts the existence of black holes, gravitational waves and novel effects like gravitational lensing and time dilation. Furthermore, GR is able to describe phenomena in astrophysics scales, and also in cosmic scales. The cosmological constant, introduced by Einstein in his Einstein field equations in 1917 [1], is originally introduced to counterbalance the effect of gravity and achieve a static universe, then abandoned after Edwin Hubble showed in 1929 [2] that the furthest galaxies are the ones that recede faster leading to the interpretation that the Universe is expanding. A precise survey on supernova in 1998 discovered the universe is expanding in a accelerating manner [3], this implies the cosmological constant may have a positive value, and a new term Dark energy was introduced for this driving component of the Universe. Besides this, a new form of matter called "Dark Matter" was introduced to explain the stability of galaxies and the rate of formation of large-scale structures since the appearance of surprising observations, which are the excessive speed of the galaxies and missing mass observed in the Coma galaxy cluster, by Zwicky in 1933 [4]. Knowing that "Dark Matter"

and "Dark Energy" are known today to be a major portion of mass-energy density budget our Universe, they remain mysterious for us on what actually they are.

Another important moment in the history of cosmology included the discovery of the cosmic microwave background radiation by Arno Penzias and Robert Woodrow Wilson in 1964 [5] [6]. Around 1990, there were dramatic improvements on the observational instruments which allowed us to carry out highly precise surveys. We finally entered the age of data science, large amount of high quality data has been recorded and the efficiency of data analysis has to match up with the incoming "big data". Some of the important surveys included the observations of the microwave background radiation from COBE [7], WMAP [8] and Planck satellites [9], large recent and near-future galaxy redshift surveys such as 2dfGRS [10], SDSS [11] and Euclid [12]. These observations matched the predictions of the ΛCDM model.

1.2 ΛCDM Model

The concordance or standard Λ Cold Dark Matter (ΛCDM) cosmological model [13, 14] is a well defined, predictive and simple cosmological model (see Bull et al. 2016, for a review). It is defined by a set of simple assumptions:

1. The Universe consists of radiation (photons, neutrinos), ordinary matter (baryons and leptons), cold (non-relativistic) "Dark Matter" which govern structure formation and cosmological constant Λ the simplest form of dark energy, the entity that drives the accelerated expansion of the Universe;

2. General Relativity (Einstein 1917) is the theory that describes gravity on cosmological scales;

3. Follow the Cosmological Principle which states that the Universe is statistically homogeneous and isotropic in space at sufficiently large scales ($\gtrsim$ 100 Mpc) ;

4. As a consequence of 2. and 3. The Universe is described by a flat Friedmann-Lemaître-Robertson-Walker (FLRW) metric;

5. There are at least six independent parameters: the baryon Ω_b and cold dark matter Ω_c abundances, the Hubble constant h, the amplitude A_s and tilt n_s of primordial power spectrum of scalar fluctuations and the reionization optical depth τ ;

6. There is an inflationary epoch shortly after the big bang;

Despite the success of ΛCDM model in explaining most properties of cosmological observations like the accelerating expansion of the Universe, the angular power spectrum and statistical properties of the Cosmic Microwave Background (CMB) radiation, the matter power spectrum and statistical properties of large scale structure of the Universe and the observed abundances of different types of chemical light elements, this model is facing some inconsistencies between theoretical prediction and observations. The following list shows some of the most significant challenges [15]:

1. **The Hubble tension**: The value of Hubble constant H_0 obtained with supernova Type Ia data is measured significantly higher than that inferred using the angular scale of fluctuations of the Cosmic Microwave Background in the context of the ΛCDM model [16].

2. **The growth tension**: Direct measurements of the growth rate of cosmological perturbations (Weak Lensing, peculiar velocities, Cluster Counts) indicate a lower growth rate than that indicated by the Planck satellite in the context of the ΛCDM model [17];

3. **CMB anisotropy anomalies**: A slightly rotated polarization on the cosmic microwave background which is unexpected by the standard model [18];

1.3 Cosmological luminosity distances

The universe is under accelerated expansion, and the expansion rate can be described by the Hubble function $H(z)$, which can be expressed in term of its value today H_0 (in the units of km/s/Mpc) and a function $E(z)$ that describes the different cosmological models. We can figure out the rate of expansion by measuring different cosmological distances, such as the luminosity distance, angular distance or the luminosity distance of gravitational waves. By fitting a theoretical cosmological distance function with current observational data or mock catalogs, we are able to estimate the range allowed for the Hubble constant and other cosmological parameters.

Consider a luminous cosmological source with absolute luminosity L illustrate in Fig. (1.1), the power emitted from the source is distributed in the spherical shell with area $4\pi d_L^2$ and the power radiated by the source is conserved. Therefore, the apparent luminosity/Energy flux (F) received by the observer (white unit square) located in different distant is:

$$F = \frac{L}{4\pi d_L^2} \tag{1.1}$$

The quantity d_L is defines as the luminosity distance. However, in the case of an expanding Universe, the energy is not conserved which result from the redshift effect felt by the photons. Then the luminosity distance for a flat universe is [19]:

$$d_L(z) = c(1+z)\int_0^z \frac{dz'}{H(z')} \tag{1.2}$$

The luminosity distance is an important cosmological observable which can be measured by standard candles like Type Ia supernovae (SnIa) ($z < 2.3$) and gamma-ray bursts (GRBs) ($0.1 < z < 9$). As the characteristic light curves of Type Ia supernovae are well known and can be standardize, by measuring the luminosity as a function of time after the explosion and the redshifts of the host galaxies, the distance-redshift relation of SnIa event is obtained. One of the latest and largest SnIa dataset available is the Pantheon sample [20] consisting of a total of 1048 SnIa in the redshift range ($0.01 < z < 2.26$). We will use this dataset to compute the prior on the parameter on Ω_m and M^* in this dissertation see sections 4.2.1.

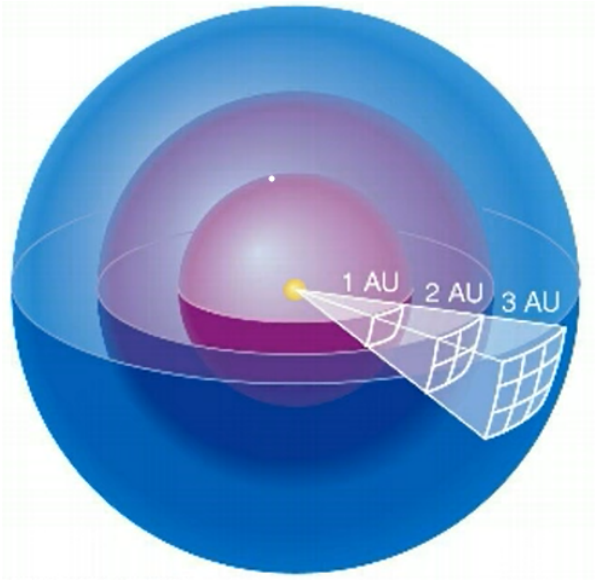

Figure 1.1: EM radiation is emitted by the point source (yellow) and the Flux received by observer located in different distances correspond to the unit square (white) in this figure

1.4 Standard Sirens: Gravitational waves + Electromagnetic (EM) counterpart

Gravitational waves (GW) are perturbations in the curvature of spacetime, generated by accelerated masses such as binary sources like black holes or neutron stars, that propagate as waves at the speed of light. This phenomenon was predicted in 1916 by Albert Einstein with his theory of general relativity [1]. Their existence was indirectly confirmed when observations of the binary pulsar in 1974 showed an orbital decay which matched the decay predicted by general relativity as the energy is lost due to gravitational radiation [21]. The first direct observation of gravitational waves was GW150914 [22], detected in 2015 by the LIGO collaboration and since then, there is a few GW events with a confirmed, GW170817 [23], and a proposed, GW190521 [24], electromagnetic (EM) counterpart. The combination of a gravitational wave (GW) signal and its independently observed EM counterpart is called a Standard Siren [25].

The first GW detection not only verified the prediction by GR, it also opened a new door to study our Universe. As an analogy, the EM observations act as the "eyes" and the GW observations act as the "ear" to receive messages from the deep space, more importantly, gravitational waves can penetrate regions of space that electromagnetic waves cannot. They allow the observation of the merger of black holes and possibly other exotic objects in the distant Universe. They also offer a possible way of observing the very early Universe, since before recombination the Universe was opaque to electromagnetic radiation. Such systems cannot be observed with traditional methods based on radiation, such as optical or radio telescopes, and so gravitational wave astronomy gives new insights on understanding the Universe. At later times when the universe is no longer opaque, we can obtain the luminosity distance for the GW and the redshift from the EM counterpart, therefore we are able to construct the Hubble diagram. In contrast to traditional standard candles, such as type Ia supernova (SnIa) calibrated by Cepheid vari-

ables, standard sirens do not require any form of cosmological distance ladder. Instead they are calibrated in the context of general relativity through the observed GW waveform [26].

In order to observe more SS events, higher sensitivity detectors are planned to launch in the coming future. With only one SS event confirmed, it is not possible at the moment to provide any parameter constraints on models. However, in what follows, we will perform forecasts by generating SS realistic mock catalogs based on the current and future GW observatories.

1.5 This thesis

1.5.1 Objectives

The main goals of this dissertation are to:

1. Study how a cosmological models based on non-metricity modify the propagation of gravitational waves ;
2. Generate mock catalogs of SS events based on current and future GW detectors;
3. Perform the parameter constraint based on two specific form of non-metricity cosmological models, namely $f(Q) = Q^n$ with $n = 1/2$ and $n = 2$, using FM method;
4. Analyze both cosmological models and determine whether future SS events will be able to distinguish between these models and ΛCDM;
5. Study the capability of higher order terms in the Fisher Matrix approach, the DALI method, for parameter estimation, when the likelihood departs from a Gaussian distribution.

1.5.2 Layout of this dissertation

This dissertation consists of 6 chapters. The first three introduce all the background information needed to make the parameters constraint in chapter 4. Chapter 5 provide a demonstration of the higher order term of Fisher Matrix method. The details of each chapter is as follows:

- Chapter 1 introduce a brief history of cosmology, which lead to the appearance of the ΛCDM model, the assumptions of this model and the problems it is facing leading to the introduction of the idea of Modified gravity;
- Chapter 2 introduces the mathematical tools used in General Relativity and the framework of non-metric theories of gravity, also the cosmological assumptions that the universe models follow and equations that govern these modified gravity model and an explanation on the propagation of gravitational wave and some essential observables;
- Chapter 3 presents the mathematical tools that compute the likelihood of the cosmological parameters on a model, which lead to the conventional method, namely the grid method. Next, we explains the theory and the properties of Fisher Information Matrix which give

an analytical simplification on the grid method. Then, we demonstrate the code implementation for the grid method and Fisher Matrix method. In the end, we provide information about the sensitivity of the observatories and the corresponding probability distribution function of the SS events, which allow us to generate realistic mock catalogs;

- Chapter 4 will show the forecast on the parameter constraints based on two specific forms of non-metricity cosmological models, namely $f(Q) = Q + MQ^n$ with $n = 0.5$ and $n = 2$, using the Fisher Matrix method. For the first model, we show a consistent result with [27] computed using Markov Chain Monte Carlo (MCMC) method;

- Chapter 5 presents an extension on the Fisher Matrix formalism which included the higher order terms, namely doublet-DALI approximation, and demonstrate the proper parameter constraints which are highly non-Gaussian.

- Chapter 6 give a summary on this dissertation and presents some foreseeable future work.

Chapter 2

Modifications of General Relativity

In this chapter, we will see how the description of gravity can be generalized and evaluate how it affects quantities such as luminosity distance for supernovae and for gravitational waves data analysis.

2.1 Geometrical Tools for GR

The spacetime metric tensor $g_{\mu\nu}$ is symmetric and depends on time and space:

$$g_{\mu\nu} = g_{\mu\nu}(t, \mathbf{x}) \tag{2.1}$$

It plays a fundamental role in General Relativity and turns observer-dependent coordinates $x^\mu = (t, x^i)$ into the invariant line element:

$$ds^2 = g_{\mu\nu} dx^\mu dx^\nu \,. \tag{2.2}$$

where Einstein notation is used (repeated indices represent summations over indexes).

The square of the length of a contravariant vector V^μ is [28]:

$$V^2 = g_{\mu\nu} V^\mu V^\nu \,. \tag{2.3}$$

The metric can also be use to find the angle between two contravariant vectors V^μ and U^ν [28]:

$$\cos(V, U) = \frac{g_{\mu\nu} V^\mu U^\nu}{\sqrt{g_{\mu\nu} V^\mu V^\nu g_{\rho\sigma} U^\rho U^\sigma}} \,. \tag{2.4}$$

The determinant of the metric is denoted by:

$$g \equiv \det(g_{\mu\nu}) \tag{2.5}$$

If the metric is non-singular and g is non-zero, then the inverse of $g_{\mu\nu}$, $g^{\mu\nu}$ is given by

$$g_{\alpha\nu} g^{\nu\beta} = \delta^\beta_\alpha \,. \tag{2.6}$$

When a vector in a Euclidean space is parallel transported around a loop, it will again point in the initial direction after returning to its original position. However, this is not true in a general Riemannian manifold. If we parallel transport a contravariant vector $V(x)$ from x to δx, the change of the vector, $\delta\tilde{V}$, can be related by the connection, Γ;

$$\delta\tilde{V}^{\mu}(x) = \Gamma^{\mu}{}_{\alpha\beta} V^{\alpha}(x) \delta x^{\beta} \,. \tag{2.7}$$

When taking the displacement to zero allow us to define the covariant derivative of a general tensor as:

$$\nabla_{\mu} V^{\nu\cdots}_{\alpha\cdots} \equiv \partial_{\mu} V^{\nu\cdots}_{\alpha\cdots} + \Gamma^{\nu}_{\beta\mu} V^{\beta\cdots}_{\alpha\cdots} + \cdots - \Gamma^{\beta}_{\alpha\mu} V^{\nu\cdots}_{\beta\cdots} - \cdots \tag{2.8}$$

Where $\partial_{\mu} \equiv \partial/\partial x^{\mu}$ is the partial derivative with respect to the coordinate x^{μ}. When all the components of the connection are zero we recover flat spacetime, and the covariant derivative reduces to a partial derivative.
The Riemann curvature tensor is:

$$R^{\sigma}{}_{\rho\mu\nu} \equiv \partial_{\mu}\Gamma^{\sigma}{}_{\nu\rho} - \partial_{\nu}\Gamma^{\sigma}{}_{\mu\rho} + \Gamma^{\alpha}{}_{\nu\rho}\Gamma^{\sigma}{}_{\mu\alpha} - \Gamma^{\alpha}{}_{\mu\rho}\Gamma^{\sigma}{}_{\nu\alpha} \,. \tag{2.9}$$

By contracting the first and third component of the Riemann tensor we obtain the Ricci tensor:

$$R_{\mu\nu} = R^{\alpha}{}_{\mu\alpha\nu} \,, \tag{2.10}$$

Further contraction with the metric we obtain the Ricci scalar:

$$R \equiv g^{\mu\nu} R_{\mu\nu} \,. \tag{2.11}$$

2.1.1 The Trinity of Gravity

There are two alternatives geometric interpretation in flat spacetime, that recover the formulations of General Relativity, which also follow the equivalence principle. Instead of the standard interpretation of gravity in which gravitational interaction is described in terms of the spacetime curvature, gravity can also be fully described either by torsion or by non-metricity. These three interpretations of General Relativity (GR) are known as the geometrical trinity of gravity [29]. We can summarize the different interpretations of gravity with the support of fig. 2.1 in the following form:

- Curvature: The rotation of a vector transported along a closed curve is given by the curvature (General Relativity), defined by the Riemann Curvature tensor $\hat{R}^{\mu}_{\nu\rho\sigma}$ in the caption;
- Torsion: The non-closure of parallelograms formed when two vectors are transported along each other is given by the torsion (Teleparallel Equivalent of General Relativity), defined by the torsion tensor $\hat{T}^{\mu}_{\nu\rho}$ in the caption;
- Non-metricity: The variation of the length of a vector as it is transported is given by the non-metricity (Symmetric Teleparallel Equivalent of General Relativity), defined by the non-metricity tensor $\hat{Q}^{\mu}_{\nu\rho}$ in the caption;

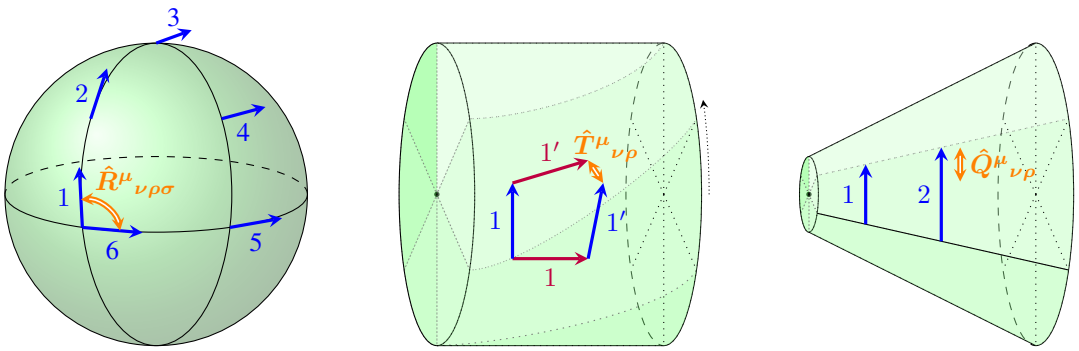

Figure 2.1: This figure illustrates the geometrical meaning of when a vector is transported along a closed curve in the respective geometry which is govern by the curvature (left), the torsion (center) and the non-metricity (right), while the remaining objects vanish. The figure is taken from [30]

The affine connection is compose of three contributions: the Levi-Civita connection, contortion and disformation,

$$\Gamma^{\lambda}{}_{\mu\nu} = \left\{{}^{\lambda}{}_{\mu\nu}\right\} + K^{\lambda}{}_{\mu\nu} + L^{\lambda}{}_{\mu\nu}\,, \tag{2.12}$$

the first term is the Levi-Civita connection which is symmetric and depend on the metric and its derivatives.

$$\left\{{}^{\lambda}{}_{\mu\nu}\right\} \equiv \frac{1}{2}g^{\lambda\beta}\left(\partial_{\mu}g_{\beta\nu} + \partial_{\nu}g_{\beta\mu} - \partial_{\beta}g_{\mu\nu}\right)\,, \tag{2.13}$$

the second term is the contortion which is related to the metric and the torsion tensor:

$$K^{\lambda}{}_{\mu\nu} \equiv \frac{1}{2}g^{\lambda\beta}\left(T_{\mu\beta\nu} + T_{\nu\beta\mu} + T_{\beta\mu\nu}\right)\,, \tag{2.14}$$

where the torsion tensor $T_{\alpha\beta\gamma}$ encodes the asymmetric part of the affine connection:

$$T^{\lambda}{}_{\mu\nu} \equiv \Gamma^{\lambda}{}_{\mu\nu} - \Gamma^{\lambda}{}_{\nu\mu}\,. \tag{2.15}$$

And the third term is the disformation:

$$L^{\lambda}{}_{\mu\nu} \equiv \frac{1}{2}g^{\lambda\beta}\left(-Q_{\mu\beta\nu} - Q_{\nu\beta\mu} + Q_{\beta\mu\nu}\right)\,. \tag{2.16}$$

where the non-metricity tensor $Q_{\alpha\beta\gamma}$ is defined as:

$$Q_{\alpha\mu\nu} \equiv \nabla_{\alpha}g_{\mu\nu} = \partial_{\alpha}g_{\mu\nu} - \Gamma^{\beta}{}_{\alpha\mu}g_{\beta\nu} - \Gamma^{\beta}{}_{\alpha\nu}g_{\mu\beta}\,. \tag{2.17}$$

As we see in Eq. (2.15), two successive covariant derivatives may not commute, meaning that when we change the order of the derivatives, the result may change according to the relation:

$$\nabla_{[\mu}\nabla_{\nu]}V^{\alpha} = \frac{1}{2}R^{\alpha}_{\beta\mu\nu}V^{\beta} + \frac{1}{2}(\Gamma^{\sigma}_{\mu\nu} - \Gamma^{\sigma}_{\nu\mu})\nabla_{\sigma}V^{\alpha}\,, \tag{2.18}$$

In the case of torsion free connection, the second term of Eq. (2.18) vanishes.

After introducing the essential quantities for recovering the equivalent theory of GR, we can see by choosing only the Levi-Civita connection in the affine connection Eq. (2.12), and neglected

the contortion and disformation tensor, the Ricci Scalar is now totally governed in terms of the Levi-Civita connection $R = \overbrace{R}^{LC}$ and we compute the equations of motion using the action:

$$S = \int \sqrt{-g} \left(\frac{c^4}{16\pi G} R + \mathcal{L}_m \right) dx^4 \,, \tag{2.19}$$

where c is the speed of light, G is the gravitational constants, $\mathcal{L}_m$ is the Lagrangian for the energy-matter content of the universe.

Then, by varying the action with respect to the metric, we obtain the standard Einstein Field Equations (EFE):

$$\overset{\text{LC}}{R}_{\mu\nu} - \frac{1}{2} \overset{\text{LC}}{R} g_{\mu\nu} = \frac{8\pi G}{c^4} \mathcal{T}_{\mu\nu} \,, \tag{2.20}$$

where $\mathcal{T}^{\mu\nu}$ is the stress energy-momentum tensor

$$\mathcal{T}^{\mu\nu} \equiv \frac{2}{\sqrt{-g}} \frac{\delta(\sqrt{-g}\mathcal{L}_m)}{\partial g_{\mu\nu}} \,. \tag{2.21}$$

This quantity gives the energy source for the spacetime curvature on the left side of the EFE.

2.1.2 Energy-Momentum Tensor and Matter Source

The requirements of isotropy and homogeneity force the energy-momentum tensor $\mathcal{T}_{\mu\nu}$ to be that of a perfect fluid given by:

$$\mathcal{T}_{\mu\nu} = (\rho c^2 + P) u_\mu u_\nu + P g_{\mu\nu} \,, \tag{2.22}$$

where ρ and P are the energy density and the pressure of the fluid, u_ν is the four-velocity relative to the observer and satisfying the normalization condition $u^\nu u_\nu = -1$.
The universe is filled with a mixture of different matter components. It is useful to classify the different sources by their contribution to the pressure:

- Matter: Matter refer to all forms of matter for which the pressure is much smaller than the energy density $P \ll \rho c^2$ ($P \approx 0$). the energy density is dominated by the mass. The first type of dust refers to "Dark matter" which is weakly interacting and therefore invisible, and contribute to most of the matter in the universe, the second one is "Baryons" which consist of ordinary matter (nuclei and electrons).

- Radiation: Radiation denote the relativistic particles, for which the pressure is about a third of the energy density, $P = \rho c^2/3$, where the energy density is dominated by the kinetic energy instead of the mass;

- Dark Energy: A mysterious energy which provided the source for the acceleration of the universe with negative pressure $P \approx -\rho c^2$. This energy density does not decrease, meaning that energy has to be created as the universe expands.

Most cosmological fluids can be parametrised in terms of a constant equation of state (EoS):

$$w \equiv \frac{P}{\rho c^2} \,, \tag{2.23}$$

This means that cold dark collisionless matter has $w = 0$, radiation has $w = 1/3$ and vacuum energy has $w = -1$. These values govern the evolution of the energy density for each component of the perfect fluid as we see later.

2.1.3 The FLRW Universe

Under the homogeneous and isotropic universe assumption described by the Friedmann-Lemaître-Robertson-Walker (FLRW) metric and considering a flat universe, the metric reads:

$$ds^2 = -c^2dt^2 + a^2(t)\delta_{uv}dx^u dx^v, \quad (u, v = 1, 2, 3) \tag{2.24}$$

where $a(t)$ is the scale factor, which is a function of the cosmic time t, this rearrangement lead to comoving coordinates $x^u = x^1, x^2, x^3$, Then the physical velocity of an object is [31]:

$$v^u_{\text{phys}} \equiv \frac{dx^u_{\text{phys}}}{dt} = a(t)\frac{dx^u}{dt} + \frac{da}{dt}x^u \equiv v^u_{\text{pec}} + Hx^u_{\text{phys}} \tag{2.25}$$

As we see there are two contributions, which are peculiar velocity, $v^u_{\text{pec}} \equiv a(t)\dot{x}^u$, and the Hubble flow, $v^u_H = Hx^u_{\text{phys}}$ where the Hubble function is defined as:

$$H \equiv \frac{\dot{a}}{a} \tag{2.26}$$

The peculiar velocity of an object is the velocity measured by a comoving observer that follows the Hubble flow. Figure 2.2 illustrates a system of coordinate that follows the Hubble flow,

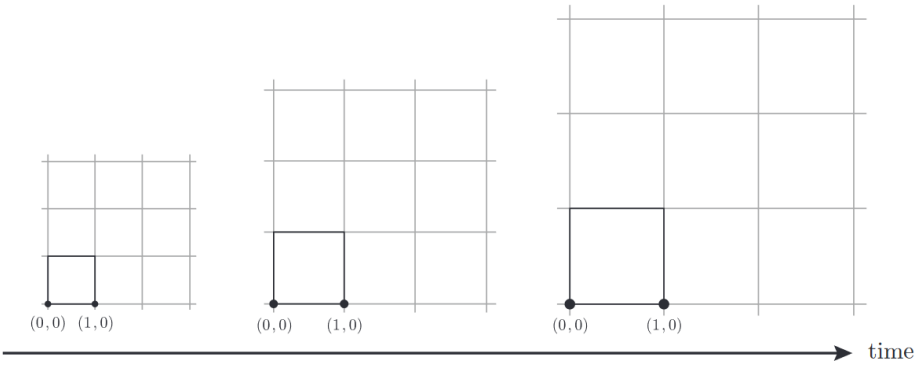

Figure 2.2: The figure illustrates the difference between comoving coordinate and physical distance between two points. The coordinates remain constant as the universe expands, whereas the physical distance increases. Figure taken from [31]

the physical distance between two points is expanding, but the coordinate remain constant. Therefore, an observer under this frame of reference able to measure the peculiar velocity of an object which deviate the Hubble flow.

2.1.4 Redshift

As information carried by light emitted from distant places and observed by us, for instance light emitted from a distant galaxy, it is essential for us to interpret the observations correctly. Therefore, we have to take into account the fact that the wavelength of the light gets stretched

due to the expansion of the universe. The wavelength of light, λ, is inversely proportional to the momentum of the photon, P, we have $\lambda = \frac{h}{P}$, where h is the Planck constant. As the momentum of photons scales as $a(t)^{-1}$, the wavelength scales as $a(t)$. As the light emitted at time t_1 with wavelength λ_1 will be observed at t_0 with wavelength:

$$\lambda_0 = \frac{a(t_0)}{a(t_1)}\lambda_1 \tag{2.27}$$

and knowing that $a(t_0) > a(t_1)$, the wavelength of the light increases, $\lambda_0 > \lambda_1$. It is conventional to define the redshift as the fractional shift in wavelength of a photon emitted by a distant galaxy at time t_1 and observed on Earth today at t_0:

$$z \equiv \frac{\lambda_0 - \lambda_1}{\lambda_1} \tag{2.28}$$

From Eqs 2.27 and 2.28 we have:

$$1 + z = \frac{a(t_0)}{a(t_1)} \tag{2.29}$$

and it is common to define $a(t_0) \equiv 1$.

2.2 $f(Q)$ Gravity

In order to tackle the problems of the ΛCDM model listed in Section 1.2, one can consider modifications to the theory of gravity. There are many ways to achieve it, one of the simplest ways is to promote the scalar quantity in the action to an arbitrary function of itself for each of the different representations of gravity in 2.1.1, R, T, Q. In this dissertation, we will focus on the Symmetric Teleparallel Gravity (STG), namely $f(Q)$ gravity, with no curvature, torsion-free, and not metric compatible connection in Eq. 2.12. The non-metricity scalar Q is [29, 32]:

$$Q \equiv -\frac{1}{4}Q_{\alpha\beta\gamma}Q^{\alpha\beta\gamma} + \frac{1}{2}Q_{\alpha\beta\gamma}Q^{\gamma\beta\alpha} + \frac{1}{4}Q_\alpha Q^\alpha - \frac{1}{2}Q_\alpha \tilde{Q}^\alpha \,, \tag{2.30}$$

and the two independent contractions of the non-metricity tensor are:

$$Q_\mu \equiv Q_{\mu\alpha}{}^{\alpha} \,, \qquad \tilde{Q}^\mu \equiv Q_{\alpha}{}^{\alpha\mu} \,. \tag{2.31}$$

The result non-metricity scalar computed using Eq. (2.30) is [33]:

$$Q = 6H^2 \,. \tag{2.32}$$

The action for $f(Q)$ gravity is:

$$S = \int \sqrt{-g}\left[-\frac{c^4}{16\pi G}f(Q) + \mathcal{L}_m\right] d^4x \,. \tag{2.33}$$

where $f(Q)$ is an arbitrary function of the scalar Q.

The field equations allow us to understand the dynamics of the universe, e.g., how the cosmological fluids govern the Hubble function and scale factor, how the fluids evolve with cosmic time. This is shown in the following paragraphs for the case of $f(Q)$ model.

Varying the previous action with respect to the metric one obtains the field equations for $f(Q)$ gravity [33]:

$$\frac{2}{\sqrt{-g}}\nabla_\alpha\left(\sqrt{-g}f_Q(Q)P^{\alpha\mu}{}_\nu\right)+\frac{1}{2}\delta^\mu_\nu f+f_Q(Q)P^{\mu\alpha\beta}Q_{\nu\alpha\beta}=\frac{8\pi G}{c^4}\mathcal{T}^\mu{}_\nu\,, \tag{2.34}$$

where the index Q denotes a partial derivative of $f(Q)$ with respect to Q, $P^{\alpha\mu\nu}$ is the non-metricity conjugate,

$$P^\alpha{}_{\mu\nu}=-\frac{1}{2}L^\alpha{}_{\mu\nu}+\frac{1}{4}(Q^\alpha-\tilde{Q}^\alpha)-\frac{1}{4}\delta^\alpha_{(\mu}Q_{\nu)}\,, \tag{2.35}$$

and $L^\alpha{}_{\mu\nu}$ is the disformation tensor. Now, inserting the FLRW flat metric and the energy-momentum tensor of a perfect fluid in the modified field equations Eq. (2.34) one obtains the modified Friedmann equations. The time-time component leads to the first modified Friedmann equation [32]:

$$6f_QH^2-\frac{1}{2}f=8\pi G\rho \tag{2.36}$$

The diagonal spatial components lead to the modified second Friedmann equation:

$$(12H^2f_{QQ}+f_Q)\dot{H}=-4\pi G\left(\rho+\frac{P}{c^2}\right) \tag{2.37}$$

To obtain the continuity equation, we take the covariant derivative of the energy-momentum tensor to get:

$$\dot{\rho}+3\frac{\dot{a}}{a}\left(\rho+\frac{P}{c^2}\right)=0 \tag{2.38}$$

This results is the same as in the ΛCDM model, meaning the cosmological fluid behaves the same way. The evolution of each component of the fluid is related to the scale factor and can also be expressed in terms of the equation of state Eq. (2.23). The continuity equation for each component then reads:

$$\frac{\dot{\rho}_i}{\rho_i}=-3\frac{\dot{a}}{a}(1+w_i)\,. \tag{2.39}$$

By solving the previous equation, we obtain the evolution of the energy density of the i-th fluid component:

$$\rho_i=\rho_{i,0}\,a^{-3(1+w_i)}\,, \tag{2.40}$$

Using the values w_i of each component in Eq. (2.23) for each component one obtains the density evolution for matter, radiation and the cosmological constant:

$$\begin{array}{ll}\rho_m=\rho_{m,0}\,a^{-3}, & \text{matter}\\ \rho_\gamma=\rho_{\gamma,0}\,a^{-4}, & \text{radiation}\\ \rho_\Lambda=\rho_{\Lambda,0}, & \text{cosmological constant.}\end{array} \tag{2.41}$$

Here the index 0 refers to present time values. We can also define cosmological parameters Ω_i for each component:

$$\Omega_i=\frac{8\pi G}{3H_0^2}\rho_{i,0} \tag{2.42}$$

For further details about the geometrical trinity of gravity, readers can find an excellent review in [29].

2.3 Propagation of Gravitational Waves

In the Introduction section we briefly discussed the origin of gravitational waves in GR, and pointed out the relevance of their observation. In this subsection we will give more details on the theoretical aspects related to the propagation of gravitational waves and how standard siren events can help us to discriminate a modified gravity model from ΛCDM.

As the sources that produce SS events are far away from the observer (the Earth), GWs can be treated as small tensorial perturbations on a flat Minkowski spacetime [34]:

$$g_{\mu\nu} = \eta_{\mu\nu} + h_{\mu\nu}\,, \tag{2.43}$$

where $\eta_{\mu\nu}$ is the Minkowski metric and $h_{\mu\nu}$ is a small perturbation with $|h_{\mu\nu}| \ll 1$.
The Minkowski metric which is the same everywhere in space and time, can be written as:

$$g_{\mu\nu} = \mathrm{diag}(-1, 1, 1, 1). \tag{2.44}$$

where diag is the diagonal elements of a matrix.
When we perform a linearization, the affine connections and Riemann curvature tensor become [35]:

$$\Gamma^{\nu}_{\mu\rho} = \frac{1}{2}\eta^{\nu\lambda}\left(\partial_\rho h_{\lambda\mu} + \partial_\mu h_{\lambda\rho} - \partial_\lambda h_{\mu\rho}\right)\,, \tag{2.45}$$

$$R_{\mu\nu\rho\sigma} = \frac{1}{2}(\partial_{\rho\nu}h_{\mu\rho} + \partial_{\rho\mu}h_{\nu\sigma} - \partial_{\rho\mu}h_{\nu\rho} - \partial_{\rho\nu}h_{\mu\sigma})\,. \tag{2.46}$$

We then introduce the trace-reverse tensor:

$$\overline{h}^{\mu\nu} = h^{\mu\nu} - \frac{1}{2}\eta^{\mu\nu}h \tag{2.47}$$

where $h = \eta_{\mu\nu}h^{\mu\nu}$ and $\overline{h} = -h$. This tensor simplifies the linearized EFEs and after computing the Riemann curvature tensor, Ricci tensor and Ricci Scalar and substitute into Eq. (2.20), one obtains the linearized EFE:

$$\Box\overline{h}_{\nu\sigma} + \eta_{\nu\sigma}\partial^\rho\partial^\lambda\overline{h}_{\rho\lambda} - \partial^\rho\partial_\nu\overline{h}_{\rho\sigma} - \partial^\rho\partial_\sigma\overline{h}_{\rho\nu} = -\frac{16\pi G}{c^4}T_{\nu\sigma} \tag{2.48}$$

where the wave operator is $\Box = \eta_{\rho\sigma}\partial^\rho\partial^\sigma$. In order to further simplify the EFE, we have to find a coordinate system such that the last three terms in the left hand side of Eq. (2.48) vanish, so we impose the Lorentz gauge $\partial_\nu\overline{h}^{\mu\nu} = 0$ and gives:

$$\Box\overline{h}_{\nu\sigma} = -\frac{16\pi G}{c^4}T_{\nu\sigma} \tag{2.49}$$

The Lorenz gauge coordinate system can be found as follows. First we perform a coordinate transformation with a small displacement field, ξ^α:

$$\begin{aligned}(ct, x, y, z) &\to (\widetilde{ct}, \widetilde{x}, \widetilde{y}, \widetilde{z})\\ x^\alpha &\to \widetilde{x^\alpha}\\ \widetilde{x^\alpha} &= x^\alpha + \xi^\alpha\end{aligned} \tag{2.50}$$

with $||\xi^\alpha|| \ll 1$ and $||\frac{\partial \xi^\alpha}{\partial x^\beta}|| \ll 1$. Using the metric transformation rule:

$$\widetilde{g_{\mu\nu}} = \frac{\partial x^\rho}{\partial \widetilde{x^\mu}} \frac{\partial x^\sigma}{\partial \widetilde{x^\nu}} g_{\rho\sigma}. \tag{2.51}$$

We then obtain the perturbation $\widetilde{h_{\mu\nu}}$ in terms of the displacement field:

$$\widetilde{h_{\mu\nu}} = h_{\mu\nu} - \xi_{\mu,\nu} - \xi_{\nu,\mu}. \tag{2.52}$$

When we combine Eq. (2.47) and Eq. (2.52), also taking into account partial derivatives along different coordinates, we obtain:

$$\partial^\nu \widetilde{\overline{h}_{\mu\nu}} = \partial^\nu \overline{h}_{\mu\nu} - \Box \xi_\mu. \tag{2.53}$$

So by choosing ξ^μ such that $\partial^\nu \overline{h}_{\mu\nu} = \Box \xi_\mu$, $\widetilde{\overline{h}_{\mu\nu}}$ satisfies Eq. (2.49). Then Eq. (2.48) is simplified to:

$$\widetilde{G_{\mu\nu}} = \frac{1}{2} \Box \widetilde{\overline{h}_{\mu\nu}} = -\frac{8\pi G}{c^4} \widetilde{T_{\mu\nu}}. \tag{2.54}$$

As we study the propagation of gravitational wave (GW)s in vacuum, we set $\widetilde{T_{\mu\nu}} = 0$, therefore the GW satisfy the wave equation

$$\Box \widetilde{\overline{h}_{\mu\nu}} = 0. \tag{2.55}$$

One of the simplest form of waves are plane waves in which their wave vectors $\boldsymbol{k}$ are orthogonal to the plane wave surfaces $k^\mu h^{TT}_{\mu\nu} = 0$, where TT refer to the transverse Traceless gauge. Also, within the Lorenz gauge we can restrict extra conditions to make the GW more obvious to visualize, by using the so called Transverse Traceless (TT) conditions. Under this gauge, starting with an observer with four velocity $U = U^\mu e_\mu$ and choose the general GW amplitude A orthogonal to the observer $A_{\mu\nu} U^\mu = 0$. Also, by choosing a frame of reference which is comoving, that is only the time component in the four velocity is non-zero, $U = (c, 0, 0, 0)$. Under these conditions, all the time components in $A_{\mu\nu}$ become zero. Suppose the plane wave propagates along the z direction $k^\mu = (\frac{\omega}{c}, 0, 0, \frac{\omega}{c})$, and also the trace of GW amplitude is zero $A^\mu_\mu = 0$. The solution is composed of a superposition of two independent polarization states in TT gauge [35]:

$$h^{TT}_{\mu\nu} = \begin{bmatrix} 0 & 0 & 0 & 0 \\ 0 & h_+ & h_\times & 0 \\ 0 & h_\times & -h_+ & 0 \\ 0 & 0 & 0 & 0 \end{bmatrix}_{\mu\nu} \cos\left(\omega(t - \frac{z}{c}) + \phi_0\right), \tag{2.56}$$

where h_+ and $h_\times$ refer to the + polarization and $\times$ polarization amplitude, ϕ_0 is an arbitrary phase. Suppose a group of point particles along a ring, when a GW passes by and interact with the particles, they oscillate (compress and expand a circle of point-like test particles). Fig. 2.3 shows the effect on these particles of the + polarization on the left hand side and the $\times$ polarization on the right hand side of the figure. The latter effect is a 45° phase shift of the former.

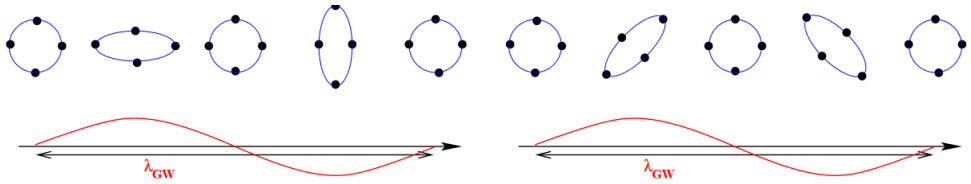

Figure 2.3: The left side of figure refers to + polarization which oscillate along time on the x-y plane, whereas the right side refers to × polarization. Figure taken from [35].

The propagation of gravitational waves in GR is given by [36]:

$$\overline{h}_A'' + 2\mathcal{H}\overline{h}_A' + k^2\overline{h}_A = 0, \tag{2.57}$$

where $\overline{h}_A$ are the Fourier modes of the GW amplitude with $A = +, \times$ refer to the two polarizations, the prime denotes the derivative with respect to conformal time η, defined as $d\eta = dt/a(t)$, and $\mathcal{H} = a'/a$.

The luminosity distance of gravitational waves under this condition behaves the same as the electromagnetic radiation governed by Eq. (1.2). However, in $f(Q)$ gravity, the coefficient of the $2\mathcal{H}$ term is modified and give propagation equation of the form [37]

$$\overline{h}_A'' + 2\mathcal{H}\left[1 - \delta(z)\right]\overline{h}_A' + k^2\overline{h}_A = 0\,, \tag{2.58}$$

where $\delta(z)$ is [38]

$$\delta(z) = -\frac{1}{2\mathcal{H}}\frac{d\ln f_Q}{d\eta}\,. \tag{2.59}$$

This can be seen as the modified Hubble function in Eq. (2.58) of the form

$$\mathcal{H}\left[1 - \delta(z)\right] = \frac{\widetilde{a}'}{\widetilde{a}} \tag{2.60}$$

The amplitude of gravitational waves instead of decaying as $1/a$, it now decay as $1/\widetilde{a}$ such that the luminosity distance for gravitational waves is [37, 36]

$$d_L^{(\mathrm{GW})}(z) = \frac{a}{\widetilde{a}} d_L^{(\mathrm{EM})}(z)\,. \tag{2.61}$$

Let us now compute this ratio $a/\widetilde{a}$. Eq. (2.60) can be rewritten as

$$\begin{aligned}
\mathcal{H}\left[1 - \delta(z)\right] &= \frac{\widetilde{a}'}{\widetilde{a}} \\
\mathcal{H}\delta &= \frac{a'}{a} - \frac{\widetilde{a}'}{\widetilde{a}} \\
&= \frac{\widetilde{a}}{a}\left(\frac{a'}{\widetilde{a}} - \frac{a\widetilde{a}'}{\widetilde{a}^2}\right) \\
&= \frac{\widetilde{a}}{a}\frac{d}{d\eta}\left(\frac{a}{\widetilde{a}}\right) \\
\frac{a'}{a}\delta &= \frac{d}{d\eta}\ln\left(\frac{a}{\widetilde{a}}\right)
\end{aligned} \tag{2.62}$$

Performing the integration of Eq. (2.62) we obtain

$$\frac{a}{\widetilde{a}} = \exp\left[\int_0^\eta \frac{a'}{a}\delta d\eta'\right] = \exp\left[\int_1^a \frac{\delta}{a} da'\right] \tag{2.63}$$

Since:

$$a = \frac{1}{1+z} \quad \rightarrow \quad da = -\frac{dz}{(1+z)^2} \tag{2.64}$$

Through the GW signal, we are able to tell the luminosity distance of GW event. It behaves similar to electromagnetic radiation which is redshifted and loses energy during the propagation in an expanding universe. Combining Eq. (2.63) and Eq. (2.64), the GW luminosity distance formulation is similar to the EM counterpart, Eq. (1.2), but consists of an additional multiplicative term [37]:

$$\frac{a}{\widetilde{a}} = \exp\left[-\int_0^z \frac{\delta}{1+z} dz\right] \tag{2.65}$$

Replacing Eq. (2.59) into Eq. (2.65), the modified GW luminosity distance gives [38]:

$$d_L^{(\mathrm{GW})}(z) = \sqrt{\frac{f_Q^{(0)}}{f_Q}} d_L(z)\,, \tag{2.66}$$

where $f_Q^{(0)}$ is the function f_Q computed at the present day.

Chapter 3

Methodology

In this chapter we introduce the approaches to perform χ^2 test to compute the likelihood of parameters of a model fitting either real or mock data. The first approach is the grid method and the second is the Fisher Matrix Method which is the main focus of this dissertation. We explain how to study our cosmological models using Type Ia Supernovae data and mock data of Standard Sirens. Then, we explain the theory of FM and its properties. We give an example to demonstrate the code implementation on both methods. At the end of this chapter, we provide the specifications of three types of gravitational wave observatories: Laser Interferometer Gravitational-Wave Observatory (LIGO), Laser Interferometer Space Antenna (LISA) and Einstein Telescope (ET). We explain the procedure on mock catalog generation based on these specifications.

3.1 The χ^2 test

3.1.1 Type Ia Supernovae

A type Ia supernova (SnIa) is a type of supernova explosion that occurs in binary systems, when one of the stars is a white dwarf that accretes mass from its companion beyond the Chandrasekhar limit which is 1.44 solar masses. This type of supernovae are used as standard candles which means for a given cosmological model it is possible to measure the distance of their host galaxy from their standarizable light curves. In this work, we utilize the SnIa events from the Pantheon sample available in the public repository [20]. In order to reduce the computational time, the binned version is considered throughout this dissertation and provided the same result as the complete dataset. Next, to quantify how likely a theoretical model $f_i(p)$ with a set of parameters p, fit a set of data y_i , we compute χ^2:

$$\chi^2 = \sum_{i=1}^{N} \left[\frac{(f_i(p) - y_i)}{\sigma_i} \right]^2 \tag{3.1}$$

In the case of SnIa event, the χ^2 equation becomes [39]:

$$\chi^2 = \sum_{i=1}^{N} \left[\frac{m^{(\mathrm{obs})}(z_i) - m^{(\mathrm{th})}(z_i)}{\sigma(z_i)} \right]^2 , \tag{3.2}$$

where $m^{(\mathrm{obs})}$ is the observed apparent magnitude, $m^{(th)}$ is the theoretical prediction for the apparent magnitude, N the total number of SnIa events and finally z_i and $\sigma(z_i)$ are the redshift

and the total uncertainty of the i-th observation, respectively. The relationship between the apparent magnitude and the luminosity distance is given by [39]:

$$m^{(th)} = M + 5\log\left(d_L(z)\right) + 25 \tag{3.3}$$

where M is the bolometric magnitude and d_L is in the units of Mpc. Let us introduce the following rearrangement considering the numerator of Eq. (3.2),

$$\begin{aligned}\Delta &= m_{\rm th} - m_{\rm obs} \\ &= M + 25 + 5\log\left(d_L(z)\right) - m_{\rm obs} \\ &= M + 25 + 5\log\left(\frac{c}{H_0}D_L(z)\right) - m_{\rm obs}\end{aligned} \tag{3.4}$$

where

$$d_L(z) = \frac{c}{H_0}D_L(z) \tag{3.5}$$

where $D_L(z)$ is the dimensionless luminosity distance.

$$\begin{aligned}\Delta &= \overbrace{M + 25 + 5\log\left(\frac{c}{H_0}\right)}^{\mathcal{M}} + 5\log(D_L) - m_{\rm obs} \\ &= \mathcal{M} + 5\log\left(D_L(z)\right) - m_{\rm obs} \\ &= \mathcal{M} + \widetilde{\Delta} \quad \text{where} \quad \widetilde{\Delta} = 5\log D_L(z) - m_{\rm (obs)}\end{aligned} \tag{3.6}$$

where $\mathcal{M} = M + 25 + 5\log\left(\frac{c}{H_0}\right)$. Using $\mathcal{M}$ in Eq. (3.3), $m_{\rm th}$ can be written as

$$m_{\rm th} = \mathcal{M} + 5\log\left(D_L(z)\right), \tag{3.7}$$

and

$$D_L(z) \equiv \frac{H_0}{c}d_L(z) = (1+z)\int_0^z \frac{1}{E(z)}dz\,, \tag{3.8}$$

where $E(z) \equiv H(z)/H_0$, $H_0 \equiv H(a = a_0 = 1)$ is the Hubble constant. The latter is typically written as $H_0 = 100h\,\mathrm{km\,s^{-1}Mpc^{-1}}$, where h refers to the dimensionless Hubble constant also known as Hubble parameter.

As we noticed from Eq. (3.5), $d_L(z)$, which is H_0 dependent, manifests a degeneracy between H_0 and M. This "unwanted" degeneracy can be resolved by using D_L which is H_0 independent, and take $\mathcal{M}$ as a nuisance parameter. If no prior knowledge of $\mathcal{M}$ at all is assumed, we can integrate the general χ^2 function over $M \in]-\infty, \infty[$ or equivalence to say, fix the χ^2 function at its minimum value. This is shown in the following steps. Lets insert Eq. (3.6) in the χ^2 equation which yields:

$$\chi^2 = \sum_{i=1}^{N}\frac{\Delta_i^2}{\sigma^2(z_i)} = \sum_{i=1}^{N}\frac{(\mathcal{M} + \widetilde{\Delta_i})^2}{\sigma^2(z_i)} = \sum_{i=1}^{N}\left[\frac{\widetilde{\Delta}^2(z_i)}{\sigma^2(z_i)} + 2\frac{\widetilde{\Delta}(z_i)\mathcal{M}}{\sigma^2(z_i)} + \frac{\mathcal{M}^2}{\sigma^2(z_i)}\right]. \tag{3.9}$$

We now define A, B and C, for further simplification of Eq. (3.9),

$$A \equiv \sum_{i=1}^{N}\frac{\widetilde{\Delta}^2(z_i)}{\sigma^2(z_i)}\,, \qquad B \equiv \sum_{i=1}^{N}\frac{\widetilde{\Delta}(z_i)}{\sigma^2(z_i)}\,, \qquad C \equiv \sum_{i=1}^{N}\frac{1}{\sigma^2(z_i)}\,. \tag{3.10}$$

to obtain:

$$\chi^2 = A + 2B\mathcal{M} + \mathcal{M}^2 C\,, \tag{3.11}$$

Fixing the χ^2 at its minimum with respect to $\mathcal{M}$:

$$\frac{d\chi^2}{d\mathcal{M}} = 0, \qquad 2\mathcal{M}C + 2B = 0 \qquad \Rightarrow \qquad \mathcal{M} = -\frac{B}{C} \tag{3.12}$$

$$\chi^2 = \left(\frac{B}{C}\right)^2 C - 2\frac{B}{C}B + A = -\frac{B^2}{C} + A \tag{3.13}$$

The likelihood for the SnIa then becomes [40]:

$$\mathcal{L} = \; A' \exp\left[-\frac{1}{2}(-B^2/C + A)\right] \; . \tag{3.14}$$

where A' is a normalization factor.

By using Eq. (3.14), and by seting up a mesh-grid of parameter values, one can compute parameter constraints using supernova data. This method is called grid method. And the usage of SnIa data is a complement of the constrains set by SS events due to a degeneracy between Ω_m and a cosmological parameters that appears in the $f(Q)$ theory.

3.1.2 Standard Sirens

A standard siren (SS) event is a compact binary system whose merger, emitted both gravitational waves and electromagnetic radiation due to the loss of energy from the system. The spectrum allows us to obtain the redshift and the luminosity distance of the source. By constructing a relation of luminosity distance as a function of redshift, we can constrain cosmological parameters and test the evolution of the universe.

The formulation of the likelihood with respect to Gravitational Wave luminosity is also based on Eq. (3.1), which is now written as [27]:

$$\mathcal{L} = \prod_{i=1}^{N} \frac{1}{\sqrt{2\pi}\sigma_{\rm tot}(z_i)} \exp\left(-\frac{1}{2}\left[\frac{d_{\rm GW}^{\rm (obs)}(z_i) - d_{\rm GW}^{\rm (th)}(z_i)}{\sigma_{\rm tot}(z_i)}\right]^2\right) , \tag{3.15}$$

where $d_{\rm GW}^{\rm (obs)}(z_i)$ and $d_{\rm GW}^{\rm (th)}(z_i)$ are the i-th observed and the theoretical luminosity distance predicted by a model in redshift z_i respectively. N is the number of SSs events. The parameter constraints for GW luminosity distance is done using both the grid method and a Fisher Matrix methodology in Chapter 4.

3.2 Fisher Information Matrix

3.2.1 Bayesian Inference Methodology

In cosmology, the focus is on testing models that aim to describe the Universe. Statistical tools are then used to estimate the probability function for the parameters of these models based on observational data. One of those statistical tools is the fisher matrix method [41], which is the main focus in this dissertation. This chapter introduces the method along with its properties. Additionally, detailed steps for code implementation are provided to demonstrate its practical application.

3.2.2 Statistical Inference

In forward probability (The frequentist approach) the goal is to compute the probability distribution of the data given a fixed and "true" value of the parameters. Data is often taken as described by random Gaussian variables. Their probability corresponds to the frequency of a given outcome occurs after many repetitions of the experiment, since the sample size of the data is suppose to be large, meaning that the distribution is Gaussian.

In Inverse Probability (The Bayesian approach), the parameters are unobserved random variables, and have a probability distribution function. The goal is to compute the conditional probability of a model given a data set $P(m|d)$. The joint probability $P(m,d)$ can be defined in both ways: $P(m,d) = P(m|d)P(d)$ or $P(m,d) = P(d|m)P(m)$, where the data (the estimated physical property) denoted as d, the model (the values of the parameters) denoted as m. Combining these expressions one has:

$$P(m|d) = \frac{P(d|m)P(m)}{P(d)} \tag{3.16}$$

This is known as the Bayes Theorem. The conditional probability $P(m|d)$ is known as the posterior probability distribution function. The function $P(d|m)$ is usually referred as the likelihood function. The function $P(m)$ is known as the Prior distribution function as it encodes prior information about the parameters. The $P(d)$ is known as Evidence and gives the probability of the data. It may be obtained from the joint probability by integrating over the full range of parameter values. That is marginalizing over all parameters,

$$P(d) = \int_m P(d|m)P(m). \tag{3.17}$$

which means that is model independent and therefore constant for a given dataset.

In frequentist hypothesis test, the crucial information we want to know is the χ^2 distribution of $P(d|m)$ that transmits how good is the data to fit a given model. While in Bayesian parameter inference, the crucial information we want to know is the χ^2 distribution P(m|d) which is how good is the variation of models fits for a given data set. As we see from Eq. (3.16), one has $P(d|m) \propto P(m|d)$ if there is no prior information about the model ("uniformative" prior). So there are two spaces exist and interrelated: the data space and the parameter space show in Figure (3.1). From the fisher matrix derivation show in the next subsection, we can understand how we perform a transformation from the data space to the parameter space.

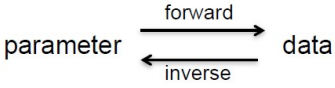

Figure 3.1: This figure shows the relation between parameter space and the data space

To estimate the parameter values and their uncertainties from data, we need to the posterior distribution $P(m|d)$ which lives in the parameter's space. There are three general ways to do this:

1. By direct computation of the likelihood on a grid

2. By stochastic methods such as Monte Carlo.

3. Fisher matrix.

3.2.3 Fisher information matrix

To calculate the likelihood function of a model using a grid method is often computationally expensive. For instance, a model with 10 parameters and considering 10 values in each dimension, implies that the evaluation of the likelihood demands 10^{10} calculaions. There are faster methods like the Monte Carlo approach which instead of evaluating a full grid, one explores the log Likelihood function with random jumps, where the size of the jump is related to the steepness of the function. Smaller jumps over rough paths, larger jumps over flatlands. With this technique, que number of evaluations grow with the number D of dimensions (parameters), instead of exponentially as in the full grid method. The Fisher matrix is a way to compute the likelihood even faster, with just a few of tens of calculations.

Theory

Suppose we obtain a series of observations y_i, $i \in 1, ..., B$, where B is the total number of data points. Let us assume the data y_i can be modeled by a function f_i with some parameters p in the bin i. One can define the χ^2 function as:

$$\chi^2 = \mu_i C^{-1}_{ij(data)} \mu_j \tag{3.18}$$

where $\mu_i = f_i(p) - y_i$, and $C^{-1}_{ij(data)}$ is the inverse of the data covariance matrix:

$$C_{(data)} = \begin{bmatrix} \sigma_1^2 & \sigma_{12} & ... & \sigma_{1B} \\ \sigma_{21} & \sigma_2^2 & ... & \sigma_{2B} \\ \vdots & \vdots & ... & \vdots \\ \sigma_{B1} & \sigma_{B2} & ... & \sigma_B^2 \end{bmatrix} = \begin{bmatrix} \sigma_1^2 & \rho_{12}\sigma_1\sigma_2 & ... & \rho_{1B}\sigma_1\sigma_B \\ \rho_{21}\sigma_2\sigma_1 & \sigma_2^2 & ... & \rho_{2B}\sigma_2\sigma_B \\ \vdots & \vdots & ... & \vdots \\ \rho_{B1}\sigma_B\sigma_1 & \rho_{B2}\sigma_B\sigma_2 & ... & \sigma_B^2 \end{bmatrix} \tag{3.19}$$

where ρ_{ij} is the correlation coefficient between the variables y_i and y_j, σ_i^2 is the variance of y_b.

If observations are uncorrelated, meaning that one observation does not affect the measurement of the other observations, then the covariance matrix becomes diagonal, $C_{(data)} = \text{diag}(\sigma_1^2, ..., \sigma_B^2)$, and the χ^2 function reads:

$$\chi^2 = \sum_{i=1}^{B} \frac{(f_i(p) - y_i)^2}{\sigma_i^2} \tag{3.20}$$

From the χ^2 one can define the likelihood function of the parameters as:

$$L(p) \propto \exp\left(-\frac{1}{2}\chi^2\right) \tag{3.21}$$

Once again, by the central limit theorem, the distribution is Gaussian. For instance, see figure 3.2 and the fiducial value of the parameters located at (0,0). The smaller the value of χ^2, the larger is the likelihood occur on that value of parameters. Since the Fisher matrix method is a Taylor series expansion up to second order to approximates only the region near the maximum of

the likelihood, therefore the Fisher matrix method is usually used in forecasts where we already know which are the parameter values that lead to a maximum likelihood. In addition, the Fisher Matrix method is only valid if the contour levels are ellipses, or in other words, that we do have a Gaussian likelihood.

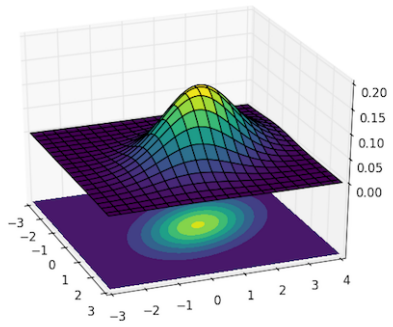

Figure 3.2: Example: Gaussian distribution in 2 dimensional parameter space

If we expand about the best guess fiducial values of the parameters, which is $p_i = p_{i(fid)} + \delta p_i$, using a Taylor expansion to the second order and take the average over the data set. We obtain:

$$\langle \chi^2(p) \rangle = \langle \chi^2(p_{fid}) \rangle + \left\langle \frac{\partial \chi^2(p_{fid})}{\partial p^j} \right\rangle \delta p^j + \frac{1}{2} \left\langle \frac{\partial^2 \chi^2(p_{fid})}{\partial p^j \partial p^k} \right\rangle \delta p^j \delta p^k + ... \tag{3.22}$$

The first term is a constant value, the second term (first derivative) vanishes, since taking the average over the data points in bin b, the mean value of the gaussian distribution falls on the theoretical curve. This implies:

$$\left\langle \frac{\partial \chi^2(p_{fid})}{\partial p_j} \right\rangle = \sum_{b=1}^{B} \frac{2(f_b(p_{fid}) - \overbrace{\frac{\sum_{i_b} y_{i_b}}{N_b}}^{\langle y_{i_b} \rangle})}{\sigma_b^2} \frac{\partial f_b(p_{fid})}{\partial p_j} = 0 \tag{3.23}$$

where N_b is the number of data point in bin b. So the shape of the distribution is encoded in the third term. We therefore define the Fisher matrix as [41]:

$$F_{jk} = \frac{1}{2} \left\langle \frac{\partial^2 \chi^2(p_{fid})}{\partial p^j \partial p^k} \right\rangle \tag{3.24}$$

Moreover, the second derivative of χ^2 along the parameters reduce to first derivatives of the fiducial model due to the averaging of different data sets:

$$\left\langle \frac{\partial^2 \chi^2(p_{fid})}{\partial p_j \partial p_k} \right\rangle = \sum_{b=1}^{B} \left(\frac{2}{\sigma_b^2} \frac{\partial f_b(p_{fid})}{\partial p_k} \frac{\partial f_b(p_{fid})}{\partial p_j} + \frac{2 \overbrace{(f_b(p_{fid}) - \langle y_{i_b} \rangle)}^{0}}{\sigma_b^2} \frac{\partial^2 f_b(p_{fid})}{\partial p_j \partial p_k} \right) \tag{3.25}$$

Therefore we obtain the Fisher matrix in terms of the first derivative [42]:

$$F_{jk} = \sum_{b=1}^{B} \frac{1}{\sigma_b^2} \frac{\partial f_{b(fid)}}{\partial p^j} \frac{\partial f_{b(fid)}}{\partial p^k} \tag{3.26}$$

and the covariance matrix of the parameters is simply the inverse of the Fisher matrix

$$\left\langle \delta p^j \delta p^k \right\rangle = (F^{-1})^{jk} \tag{3.27}$$

As we compare eq. (3.24) and eq. (3.26) , we transformed the χ^2 from data space to parameter space. The Fisher matrix offers a best-case scenario to constrain cosmological parameters. So we developed a formalism to propagate the errors from the observational errors σ_i to the cosmological parameters. Therefore with the errors σ_i based on the expected performance of a given experiment and the fiducial model, we are already able to perform a forecast. The partial derivatives in the Fisher matrix requires only a few estimations of the likelihood for each of the parameters.

3.2.4 Properties of the Fisher Matrix

Transformation of variables

We can write a Fisher matrix in terms of the new parameters p' in terms of the original Fisher matrix written in terms of p, by using the transformation matrix M_{ij}, which is the Jacobian of the transformation. We can obtain a new Fisher matrix as follows [43]:

$$F'_{mn} = \sum_{ij} \frac{\partial p_i}{p'_m} \frac{\partial p_j}{p'_n} F_{ij} \tag{3.28}$$

Also we can compute it using the matrices form:

$$[F'] = [M]^T [F][M] \quad \text{where} \quad M_{ij} = \frac{\partial p_i}{\partial p'_j} \tag{3.29}$$

Maximization of the likelihood function:

To perform maximization of the likelihood with respect to some parameters, we have to fix one of the parameters at its maximum likelihood estimator. This means putting the difference $p_i - p_{i(fid)} = 0$. This can be done by removing the rows and columns of the corresponding parameters we wish to perform maximization in the Fisher matrix. This can be illustrated by the following example. Let us consider a general two-dimensional probability distribution function (PDF) in matrix form (likelihood function in the parameter space):

$$L(P_i) = N \exp\left[-\frac{1}{2}\left(\Delta P_i C^{-1}_{ij(par)} \Delta P_j\right)\right] \tag{3.30}$$

where N is a normalization factor, $\Delta P_i = p_i - p_{i(fid)}$ and for simplification, assume $p_{i(fid)} = 0$. Similarly to Eq. (3.19), the covariance matrix of the parameter are in the form of [43]:

$$C_{(par)} = \begin{bmatrix} \sigma_1^2 & \sigma_{12} \\ \sigma_{12} & \sigma_2^2 \end{bmatrix} = \begin{bmatrix} \sigma_1^2 & \rho\sigma_1\sigma_2 \\ \rho\sigma_1\sigma_2 & \sigma_2^2 \end{bmatrix} \tag{3.31}$$

where σ_1 and σ_2 are the 1σ value of the parameters p_1 and p_2 respectively (marginalizing over the other). $\sigma_{12} = \rho\sigma_1\sigma_2$ where ρ is known as the correlation coefficient. It varies from 0 (independent) to 1 (completely correlated), both in positive and negative value. Figure 3.3 below illustrate the idea.

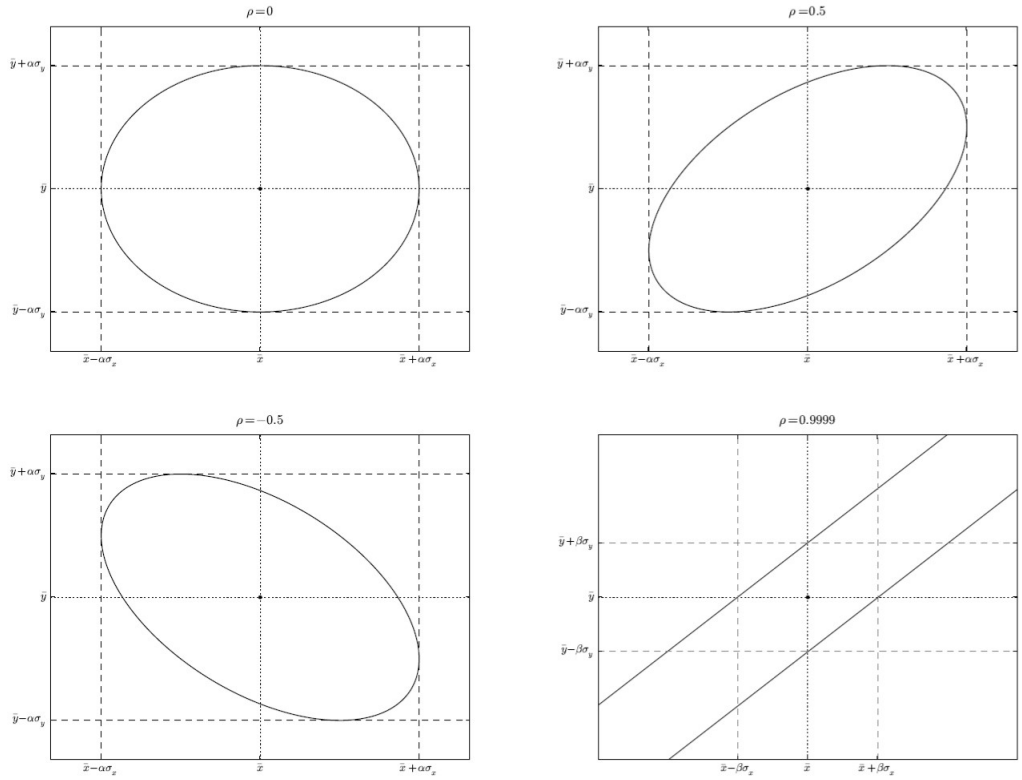

Figure 3.3: 68.3% (1-σ) confidence ellipses for parameters x and y with 1-σ uncertainties σ_x and σ_y and correlation coefficient ρ. In the first three panels, dashed lines represent the marginalized 1-σ uncertainty for each variable: $\alpha\sigma_x$ and $\alpha\sigma_y$, where $\alpha \approx \sqrt{2.3} \approx 1.52$. In the bottom-right panel, a zoom in to show the intersections with the axes: $\pm\beta\sigma_x$ and $\pm\beta\sigma_y$, where $\beta \approx 2.13\sqrt{1-\rho}$ (for $\rho \approx 1$). Figure taken from [43].

When we combine eq. (3.30) and eq. (3.31), we obtain:

$$L(p_1, p_2) = N \exp\left[-\frac{1}{2(1-\rho^2)}\left(\frac{p_1^2}{\sigma_1^2} + \frac{p_2^2}{\sigma_2^2} - 2\frac{\rho p_1 p_2}{\sigma_1\sigma_2}\right)\right] \tag{3.32}$$

As we see eq. (3.32), the term inside the bracket above the exponential encode the shape of the contour levels of the likelihood function, that is the shape of the ellipse: the length of (semi-major axis, semi-minor axis), and the angle tilted between the semi-major axis and the x-coordinate axis. Now, let us marginalize the parameter p_2, we integrate $L(p_1, p_2)dp_2$ over the whole domain. This gives:

$$L(p_1) = \hat{N} \exp\left(-\frac{p_1^2}{2\sigma_1^2}\right) \tag{3.33}$$

where $\hat{N}$ is a new normalization constant. The new correlation matrix remain only the $C_{11} = \sigma_1^2$ component, so we realize that the marginalization can be carried out by the removal of the rows and columns of the second parameter from $F^{-1} = C_{(par)}$. This procedure can be applied to any

number of dimensions. If we are interested in obtaining the fully marginalized 1σ errors of the corresponding i-th parameters , we just have to marginalize over all the others parameters:

$$\sigma_i^2 = (F^{-1})_{ii} \tag{3.34}$$

This property is one of the time-saving feature of the Fisher method. One of the examples using marginalization is, for instance, in the linear regression. If we recorded a bunch of data and derived a fit, but we are interested only in placing confidence limits on the slope and not in the intercept, then the intercept can be considered a nuisance parameter, and we should marginalize over all possible values of this parameter.

3.3 Procedure on code Implementation for the grid method and Fisher Matrix method

To demonstrate the idea, we use a simple model with 2 parameters a and b for parameter constraint computation, and applications in cosmology will be made in chapters 6 and 7. Suppose the model is a quadratic function with fiducial values $a_{fid} = 2$ and $b_{fid} = 3$:

$$y = ax^2 + b \tag{3.35}$$

We now generate a set of random x values within the range 0.1 to 3 and use it to generate the mock catalog using the steps shown in section 3.4 given the a_{fid}, b_{fid} and σ_b uncertainties for the corresponding x. Then, we compute the parameter constraints using the Grid Method described in section 3.3.1, and also using the Fisher Matrix approach that can be found in section 3.3.2.

3.3.1 Grid Method: Compute the χ^2 from the mock catalog

The following section shows the steps using grid method for the parameter constraints computation:

- First we create a parameter space a and b, and create 100 values for a with uniform spacing, and similarly for b. So for each grid point, we have different combinations of a and b values.
- Then, we use the set of x values of the mock catalog and σ_b values (in this case uniform uncertainties $\sigma_b = 0.7$) and compute the corresponding theoretical model values f_b for each set of parameters in the grid, and perform the χ^2 curve fitting with the mock catalog using eq. (3.20). This process is repeated for the whole parameter space.
- The next step is to find the minimum χ^2 value.
- Draw the 1σ and 2σ contours where the 1σ and 2σ contours are given by

$$\Delta\chi^2 = \chi^2 - \chi^2_{min} \tag{3.36}$$

$$1\sigma : \Delta\chi^2 = 2.3 \quad 2\sigma : \Delta\chi^2 = 6.17 \tag{3.37}$$

where these value apply to 2 dimension.

The parameter constraints are shown in fig. 3.4. So all the combination of parameters inside the purple contour give the 1σ probability around the best fit point indicated by a blue point. The yellow contour refers to the 2σ region.

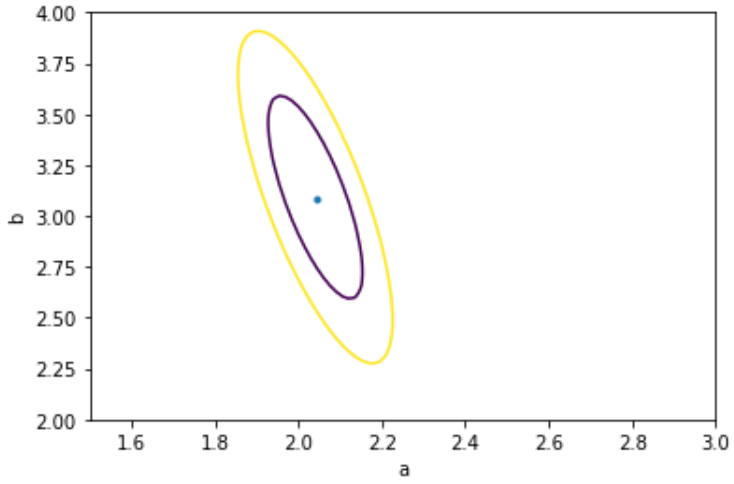

Figure 3.4: Parameter constraints computed by the Grid Method with fiducial values $a_{fid} = 2, b_{fid} = 3$

3.3.2 Fisher Matrix Method: Compute the diameter of the ellipses from the first derivatives of the model

There are different approaches to compute the Fisher matrix. The first one uses the first derivative of the model along the parameters which is the one used in this dissertation. This section shows the steps using the Fisher Matrix Method for the parameter constraints computation:

- In this model, a 2×2 array is created for the Fisher Matrix as there are two parameters a and b and no marginalization is carried out. We create two functions that perform a first derivative of our model along the corresponding parameters at the fiducial points ($a = 2$ and $b = 3$) and at every redshift values. We chose the step size of i-th parameter (Δa and Δb in this case) to be 0.01;

$$\frac{\partial f_{b(fid)}}{\partial a} = \frac{f_b(a_{fid} + \Delta a, b_{fid}, x) - f_b(a_{fid} - \Delta a, b_{fid}, x)}{2\Delta a} \tag{3.38}$$

$$\frac{\partial f_{b(fid)}}{\partial b} = \frac{f_b(a_{fid}, b_{fid} + \Delta b, x) - f_b(a_{fid}, b_{fid} - \Delta b, x)}{2\Delta b} \tag{3.39}$$

- We then compute the Fisher Matrix components following eq. (3.26) using the list of uncertainties σ_b, the two lists of numbers we generate in the previous step and also the list of uncertainties values,

- Now, we obtain four components in the Fisher matrix, and we compute the inverse of the Fisher matrix to obtain eq. (3.31). Then the ellipse parameters are calculated using the components of covariance matrix C_{par} [43]:

$$a^2_{semimajor} = \frac{\sigma_a^2 + \sigma_b^2}{2} + \sqrt{\frac{(\sigma_a^2 - \sigma_b^2)^2}{4} + c} \tag{3.40}$$

$$b^2_{semiminor} = \frac{\sigma_a^2 + \sigma_b^2}{2} - \sqrt{\frac{(\sigma_a^2 - \sigma_b^2)^2}{4} + \sigma_{ab}^2} \tag{3.41}$$

$$\tan 2\theta = \frac{2\sigma_{ab}}{\sigma_a^2 - \sigma_b^2} \tag{3.42}$$

where $\sigma_{ab} = \rho\sigma_a\sigma_b$, $a_{semimajor}$ is the length of semi-major axis, $b_{semiminor}$ is the length of semi-minor axis, θ is the angle between the semi-major axis and the x-axis.

- Now we plot the 1σ, 2σ confidence region. The axis lengths $a_{semimajor}$ and $b_{semiminor}$ are multiplied by a coefficient α depending on the confidence level one is intersected in

$$\begin{aligned} 1\sigma : \alpha &= \sqrt{\Delta\chi^2} = \sqrt{2.3} \\ 2\sigma : \alpha &= \sqrt{\Delta\chi^2} = \sqrt{6.17} \end{aligned} \tag{3.43}$$

This can be explained by the area of the ellipse:

$$A = \pi(\alpha a)(\alpha b) = \pi(\Delta\chi^2)ab \tag{3.44}$$

We then obtain the parameters constraint computed using Fisher Matrix method shown in fig. 3.5:

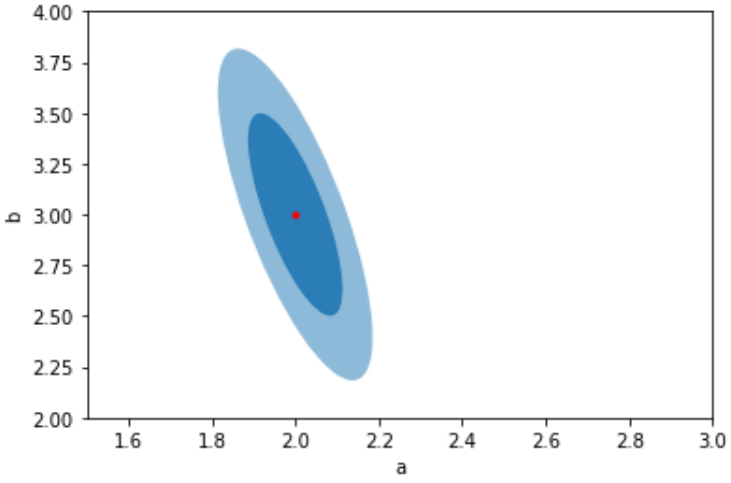

Figure 3.5: Parameter constraints computed by Fisher Matrix Method with fiducial values $a_{fid} = 2, b_{fid} = 3$

The computational speed of this method is extremely high compared to the grid method and Markov Chain Monte Carlo (MCMC), due to the analytical simplification from a second

derivative to a first derivative of the model along parameters, also by obtaining the ellipse parameters. The shape of the ellipse is obtained without loop through the parameter space and find the 1σ, 2σ region through the χ^2 values, unlike the case of higher order Fisher Matrix Method in Chapter 5.

3.4 Observatories specifications

In this dissertation, we wish to study two currently in operation gravitational wave observatories: the advanced Laser Interferometer Gravitational Wave Observatory[44], and advanced Virgo[45]; and also two future observatories: the Laser Interferometer Space Antenna, and the Einstein Telescope. The former is first space-based gravitational wave detector expected to be launched in 2037, it is aimed at the detection of massive binary events up to redshifts $z \approx 10$ using a constellation of three spacecraft arranged in an equilateral triangle with sides 2.5 million kilometres long, flying along an Earth-like heliocentric orbit. The latter is a third generation underground gravitational wave observatory expected to be build in 2035 [46], it will be able to circumvent the limitations of current advanced detectors and of their subsequent upgrades. For instance, the low frequency noise (seismic noise) lowers the sensitivity of ground base detector, ET is designed to tackle the effect of the seismic noise, and cool down the mirrors to directly reduce the thermal vibration of the test masses which enable us to reduce the uncertainties of the observation in the low redshift regime.

Before going into the detail of the specification of the observatories, we first outline the procedure for SS mock catalog generation [27]:

1. Generate random redshift z_* values following the probability distribution function of standard sirens events and the number of values is matched to the expected observed number of events for the corresponding observatory;

2. Compute the luminosity distances $d_L(z_*)$ from the obtained redshifts based on the fiducal cosmology, which is ΛCDM model, with fiducial values $h = 0.7$ and $\Omega_m = 0.284$. The latter value corresponds to the best fit for the SNIa from the Pantheon sample.

3. Compute the corresponding errors $\Delta d_L(z_*)$ for the obtained redshifts using the $\sigma_{tot}(z_*)$ for the corresponding observatory, and consider as the 1σ region for the luminosity distances;

4. Generate a sample following a Gaussian distribution with mean in $d_L(z_*)$ and with standard deviation equal to $\sigma_{tot}(z_*)$ for each obtained redshift z_* and consider this sample as the observed value of the luminosity distance $d_L^{(obs)}(z_*)$;

The following section introduce the details of LIGO, LISA and ET specifications.

3.4.1 LIGO-Virgo Forecasts

The probability distribution function of SSs events for the LIGO-Virgo observatories follow figure 2 in [47]. We first sample the values from the figure, then the PDF with respect to the luminosity distances has to be converted in terms of redshift using the chain rule $\int f(d_L)d(d_L) =$

$\int f(d_L)\frac{d(d_L)}{dz}dz$. The code first computes the luminosity distance versus redshift for a fiducial cosmology, then interpolates and reverses the function as redshift versus luminosity distance. The LIGO-Virgo catalog is composed of $N = 50$ events with a maximum redshift $z = 2$. After obtaining the PDF, we go through the steps we mentioned in the above section using the information of the uncertainties of the observatories σ_{total}. The total uncertainties of LIGO-Virgo collaboration is [48]:

$$\sigma^2_{\text{LIGO-Virgo}} = \sigma^2_{d_L} + \left(\frac{d}{dz}(d_L)\sigma_{\text{photo}}\right)^2 , \tag{3.45}$$

where σ_{d_L} is the luminosity distance measurement uncertainties, and $d_L(z)$ is in units of Mpc:

$$\sigma_{d_L} = \frac{5.63 \times 10^{-4}}{\text{Mpc}} d^2_L(z) , \tag{3.46}$$

and the second contribution is the error for the redshift, due to photometric measurements:

$$\sigma_{\text{photo}} = 0.005(1 + z) . \tag{3.47}$$

3.4.2 LISA

For the LISA mission, there are three redshift distribution of SSs events [49], which are expected to be visible to LISA. In this work we selected the distribution that provides a middle ground between the other two with respect to the redshift distribution of events, which is *No Delay* massive black hole binary (MBHB) plural population with the mission specification L6A2M5N2 since it consider as the closest proposed mission specification presented in [50]. It is expected to observe $N = 15$ SS events within the four year lifetime of LISA with redshift range above $z = 0.1$. The redshift distribution function is a beta distribution [27]:

$$f(z) = \gamma \left(\frac{z}{9}\right)^{\alpha-1} \left(1 - \frac{z}{9}\right)^{\beta-1} , \tag{3.48}$$

with values shown in the table 3.1: The normalized redshift probability distribution function is

	α	β	γ
No Delay	2.14	4.7	3.61

Table 3.1: Values of the beta distribution for the redshift distribution of the MBHB populations *No Delay* [27]

present in fig. 3.6:

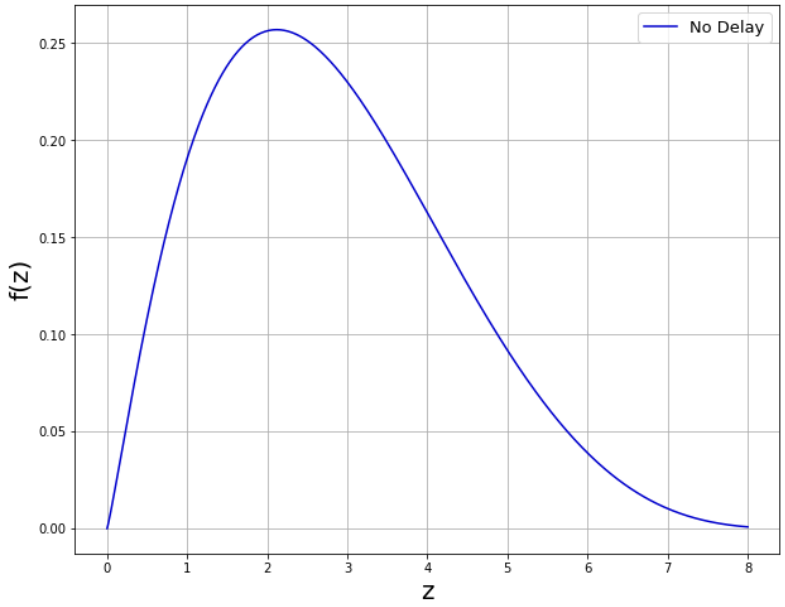

Figure 3.6: Expected normalized redshift distribution for LISA SS events with L6A2M5N2 mission specification and *No Delay* populations

The total uncertainty of the luminosity distance for LISA as a function of redshift is given by [51]:

$$\sigma^2_{\rm LISA} = \sigma^2_{\rm delens} + \sigma^2_{\rm v} + \sigma^2_{\rm inst} + \left(\frac{d}{dz}(d_L)\sigma_{\rm photo}\right)^2 , \tag{3.49}$$

The first term corresponds to total lensing uncertainty and consists of two factors in a multiplicative manner:

$$\sigma_{\rm delens} = F_{\rm delens}\,\sigma_{\rm lens}\,, \tag{3.50}$$

The delensing factor includes the possibility of estimating the lensing magnification distribution:

$$F_{\rm delens} = 1 - \frac{0.3}{\pi/2}\arctan\left(z/0.073\right), \tag{3.51}$$

and the analytically estimated weak lensing contribution:

$$\sigma_{\rm lens} = 0.066\left(\frac{1-(1+z)^{-0.25}}{0.25}\right)^{1.8} d_L(z)\,, \tag{3.52}$$

The second term refers to the error coming from the peculiar velocity of the sources:

$$\sigma_{\rm v} = \left[1 + \frac{c(1+z)^2}{H(z)d_L(z)}\right]\frac{500\ {\rm km/s}}{c} d_L(z)\,. \tag{3.53}$$

The third term considers the uncertainty in the luminosity distance measurement with the LISA instrument:

$$\sigma_{\rm inst} = 0.05\left(\frac{d_L^2(z)}{36.6{\rm Gpc}}\right), \tag{3.54}$$

The last term refers to the photometric measurements in term of luminosiy distance as a function of redshift and contribute only at redshifts larger than 2, this uncertainty is then dependent on the fiducial model.

$$\sigma_{\rm photo} = 0.03(1+z),\ \text{if } z > 2\,. \tag{3.55}$$

3.4.3 Einstein Telescope

According to [52], ET is expected to observe $N = 10^3$ SS events over a three year observation period with redshift range between $z_{\min} = 0.07$ to $z_{\max} = 2$. The observed SS events follows the normalized redshift probability distribution function:

$$f(z) = \frac{4\pi \mathcal{N} r(z) d_L^2(z)}{H(z)(1+z)^3}\,, \tag{3.56}$$

where $\mathcal{N}$ is a normalization constant, determined by the requirement that the total number of sources N_s be given by:

$$N_s = \int_{z_{min}}^{z_{max}} f(z')dz' \tag{3.57}$$

and the function $r(z)$ is called the coalescence rate which varies in redshift range:

$$r(z) = \begin{cases} 1+2z & \text{if } 0 \leq z \leq 1 \\ (15-3z)/4 & \text{if } 1 < z < 5 \\ 0 & \text{if } z > 5 \end{cases} \tag{3.58}$$

The total uncertainty consists of two contributions:

$$\sigma_{\rm ET}^2 = \sigma_{\rm inst}^2 + \sigma_{\rm lens}^2\,, \tag{3.59}$$

where

$$\sigma_{\rm inst} \approx (0.1449z - 0.0118z^2 + 0.0012z^3) d_L(z)\,, \tag{3.60}$$

is the estimate of the ET instrumental error and

$$\sigma_{\rm lens} \approx 0.05 z d_L(z)\,. \tag{3.61}$$

is the lensing error.

Chapter 4

Constraints on $f(Q)$ models

In this chapter, we computed the parameters constraints using Fisher Matrix Method for both current and future GW observatories, by using SS mock catalogs. In section 4.1 show consistence results to [27] [53] which uses an MCMC method, and section 4.2 is the original work of this dissertation. In this section we derive the $E(z)$ function and the modification of the GW luminosity distance for the polynomial $f(Q)$ model. We start from the modified first Friedmann equation presented in eq. (2.36):

$$f_Q Q - \frac{1}{2} f = 8\pi G \rho \tag{4.1}$$

with, a function f in the form stated in [54]:

$$f = Q + \alpha Q^n \,, \tag{4.2}$$

where α is a constant and Q is still $Q = 6H^2$.
We Combine Eq. (4.1) and Eq. (4.2). Since the expected SSs events are expected to be observed in late time universe, we consider it to be composed only of ordinary matter, dark matter and a cosmological constant and neglect radiation. The $E(z)$ function is:

$$E^2 + \overbrace{\frac{6^n}{3}\alpha H_0^{2n-2}}^{M^*} \left(n - \frac{1}{2}\right) E^{2n} = \frac{8\pi G}{3H_0^2}(\rho_m + \rho_\Lambda) \tag{4.3}$$

where $M^* = 6^n \alpha H_0^{2n-2}/3$ is the redefined free parameter .

Since

$$\frac{8\pi G}{3H_0^2}\rho_i^0 = \Omega_i^0 \tag{4.4}$$

We finally have:

$$E^2 + M^* \left(n - \frac{1}{2}\right) E^{2n} = \Omega_m^0 (1+z)^3 + \Omega_\Lambda^0 \tag{4.5}$$

where $\Omega_\Lambda^0 = \frac{(2n-1)}{2} M^* + 1 - \Omega_m^0$ to satisfy the condition $E(z=0) = 1$.
Knowing the GW luminosity distance is in the form Eq. (2.66), we can also written as Eq. (4.7), so we first compute:

$$G_{eff} = \frac{G}{1 + \alpha n Q^{n-1}} = \frac{G}{1 + 6^{n-1}\alpha n H(z)^{2n-2}} \tag{4.6}$$

The GW luminosity distance is:

$$\begin{aligned} d_L^{(GW)}(z,\Omega_m^0,M^*,h) &= \sqrt{\frac{f_Q^{(0)}}{f_Q}}d_L(z,\Omega_m^0,M^*,h) \\ &= \sqrt{\frac{G_{eff}(z)}{G_{eff}(0)}}d_L(z,\Omega_m^0,M^*,h) \\ &= \sqrt{\frac{1+\frac{6^{n-1}\alpha n}{H_0^{2-2n}}}{1+\frac{6^{n-1}\alpha n}{H(z)^{2-2n}}}}d_L(z,\Omega_m^0,M^*,h) \\ &= \sqrt{\frac{1+\frac{M^* n}{2}}{1+\frac{M^* n}{2}E(z,\Omega_m^0,M^*,h)^{2n-2}}}\,d_L(z,\Omega_m^0,M^*,h) \end{aligned} \tag{4.7}$$

where $E(z) \equiv H(z)/H_0$.

4.1 $n = 1/2$ model

This $f(Q)$ modified gravity cosmological model features a ΛCDM background with the differences arise in the propagation of the perturbations of gravitational waves. This difference appears from an additional free parameter theory α, and by setting its value to zero, the model gives back ΛCDM. The expression of $n = \frac{1}{2}$ model takes the form [33]

$$f(Q) = Q + \alpha\sqrt{Q}\,. \tag{4.8}$$

Starting from the first Friedmann equation presented in eq. (2.36), and set the right hand side to be equal to $3H^2$ and using the non-metricity scalar Q with its relation with the Hubble function, $Q = 6H^2$, we have:

$$Qf_Q - \frac{1}{2}f - \frac{Q}{2} = 0\,, \tag{4.9}$$

Since the SSs events are expected to be observed in late time universe and not detected at very high redshifts, therefore the universe is dominated by ordinary matter, dark matter, a cosmological constant and neglect radiation.
The Hubble function is written as:

$$H^2 = \Omega_m(1+z)^3 + \overbrace{1-\Omega_m}^{\Omega_\Lambda}\,. \tag{4.10}$$

We insert our model presented in Eq. (4.8) to the GW luminosity distance Eq. (2.66) of the $f(Q)$ model, and we obtain [27]:

$$d_L^{(GW)}(z,\Omega_m,\widetilde{M},h) = \sqrt{\frac{2\sqrt{6}+\widetilde{M}}{2\sqrt{6}+\widetilde{M}/E(z,\Omega_m)}}\,d_L(z,\Omega_m,h)\,, \tag{4.11}$$

where $\widetilde{M} = \alpha/H_0$.

As we can see there is a singularity at $\widetilde{M} = -2\sqrt{6}E(z)$ in the previous equation, therefore we have to ensure that $\widetilde{M}$ has a lower bound at $\widetilde{M} = -2\sqrt{6}$ in order to obtain a strictly physical luminosity distance for GWs, which is a real positive number for all redshifts.

4.1.1 Forecasts using Standard Sirens

As we can see, the term $\frac{\widetilde{M}}{E(z)}$ in eq. (4.11), the parameters $\widetilde{M}$ and Ω_m present in the $E(z)$ function lead to an infinite degeneracy on the parameter constraints. In order to solve this problem, we utilize Pantheon SnIa data with marginalized likelihood along H_0 to fix the value of Ω_m. The graph below show the 1σ range of Ω_m is around 0.0125 and the maximum likelihood is located around $\Omega_m = 0.284$. We then set the Ω_m value as our fiducial value, the 1σ range is then added in the $00-$component of the Fisher Matrix using this form $\frac{1}{\sigma^2_{\Omega_M}}$, this addition in the Fisher Matrices is equivalence to the multiplication of the likelihood functions. The Pantheon data provide us the Prior $P(m)$ in eq. (3.16).

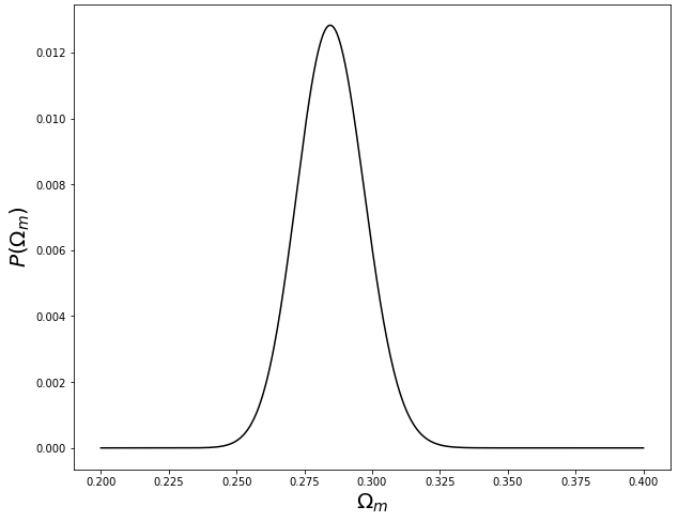

Figure 4.1: The constraint on Ω_m using Pantheon sample with the marginalized SnIa likelihood for $f(Q)$ model using eq. (3.14)

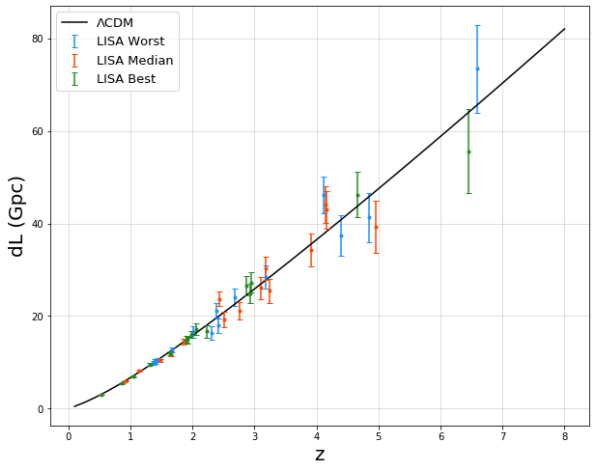

Figure 4.2: This figure shows the best, median and worst LISA catalogs represented in the luminosity distance versus redshift plane.

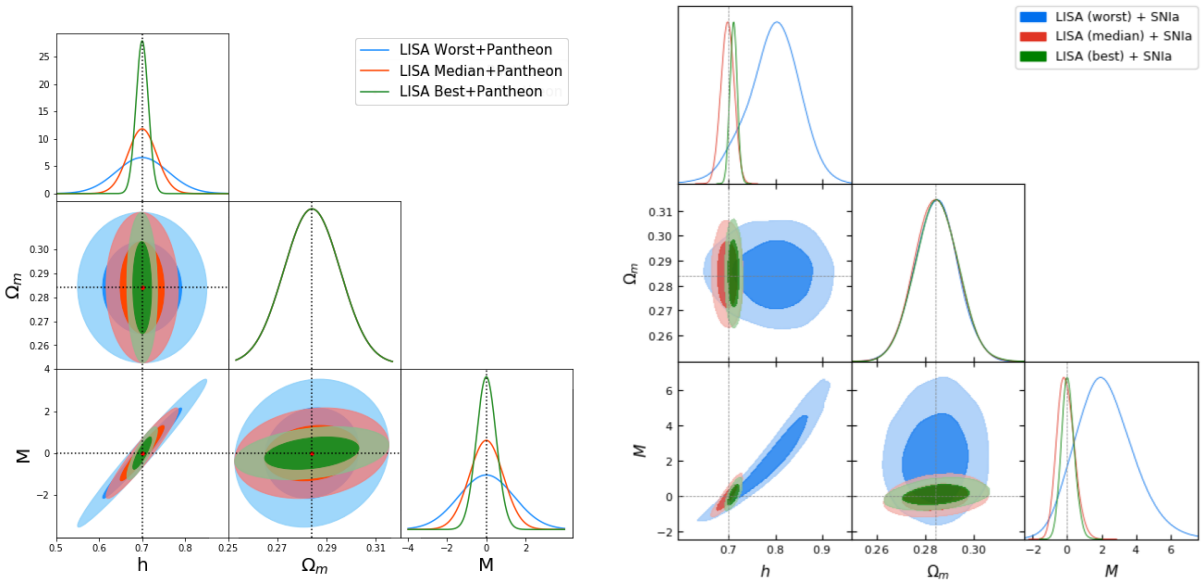

Figure 4.3: The left panel shows the corresponding constraints computed by Fisher Matrix (FM) method using the generated mock catalogs, with the Pantheon sample set on the model given by eq. (4.8). The right panel shows the parameter constraints computed by MCMC from [27]. Dotted lines represent the fiducial ΛCDM values.

LISA Forecasts

Starting the forecast with LISA, we generated three classes of catalogs with properties very similar to the results found in [27]. Figure 4.2 shows the GW luminosity distance versus redshift plane of the best, median, worst class of LISA catalogs. Some of the events happen at almost redshift $z \approx 7$.

The left panel of Fig. 4.3 illustrates the constraints on the parameters obtained by the same catalogs, computed with the Pantheon SnIa data. We can see that the constraints of the best is sufficiently better than the median, and the median is also sufficiently better than the worst case. This can be explain by noticing that the best catalogs are the ones with the largest number of low redshift data points.

Comparing the results with the ones found in ref. [27] and shown in the right panel of 4.3, we can see that the region of the constraints for three cases is very close, with the difference that the ellipses in our case are centered in the fiducial value in the Fisher Matrix method, and the computational speed is much faster compare to MCMC and grid method. This applies to all the following forecasts.

ET-Forecasts

Let us now move to the ET forecast. We have generated several sets of 1000 mock SS events, and one set of mock SS events is shown in fig. 4.4, which all give the same parameter constraints as in the left panel of fig. 4.5, and the right panel shows the parameter constraints computed by MCMC from [27]. This can be explained due to the large amount of the sample, which is sufficient enough to provide a "true" distribution. The fiducial ΛCDM cosmological model is plotted as a dashed gray line on the left panel. It shows a single ET catalog in the GW

luminosity distance versus redshift plane. The right panel shows the corresponding constraints combined with SnIa obtained from the Pantheon sample.

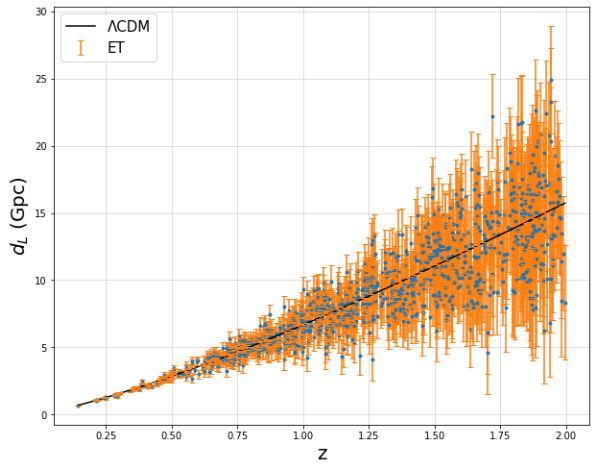

Figure 4.4: This figure refer to the 1000 SS mock events luminosity distance versus redshift relation, with mean values indicated in blue dots and the correspond uncertainties with orange bars.

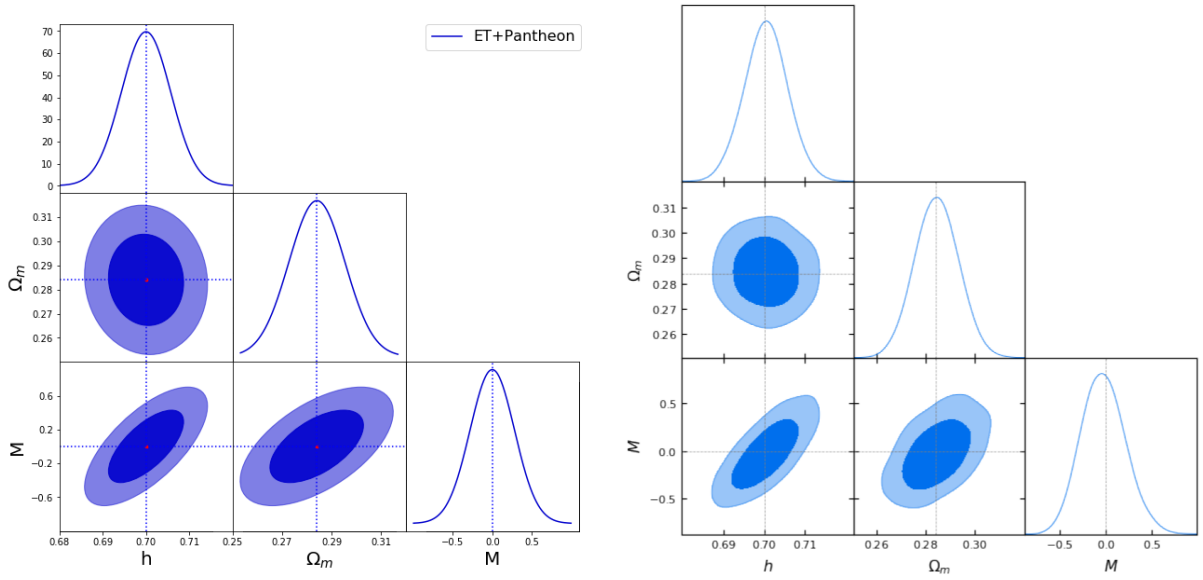

Figure 4.5: The left panel shows the parameter constraints computed by FM method, using the generated 1000 SS events with the Pantheon data on the model given by eq. (4.8). The right panel shows the parameter constraints computed by MCMC from [27]. Dotted lines represent the fiducial ΛCDM model/values

Now, we are interested in comparing the constraints between the ET forecast and the LISA's best case. The left panel of fig. 4.6 shows both catalogs and the right panel plot the constraints from the corresponding mock catalogs and the Pantheon sample. The constraints computed using Fisher matrix is slightly larger than those computed by MCMC method [27]. As we can see a larger number of low redshift events are supposed to be detected with ET when compared with LISA. At the end of 3th year operation, ET can provide a good constraint on the model, however, LISA detects fewer then 15 events and some of the events may be observed in high

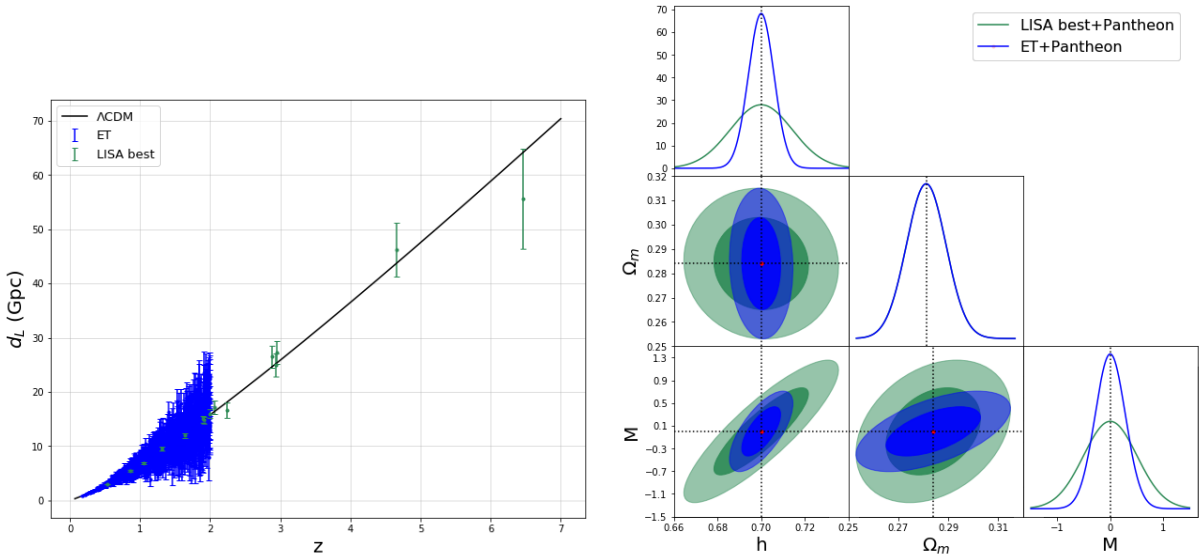

Figure 4.6: The left panel shows the luminosity distance versus redshift of ET catalog in orange and best LISA catalog in blue. The right panel shows the corresponding constraints computed by FM method combine with the Pantheon sample set on the model given by eq. (4.8). Dotted line represent the fiducial ΛCDM model/values.

redshift which further enlarge the constraint of the current forecast.

LIGO-Virgo Forecasts

For LIGO-Virgo alone is unable to provide useful constraints on the model. This can be explained

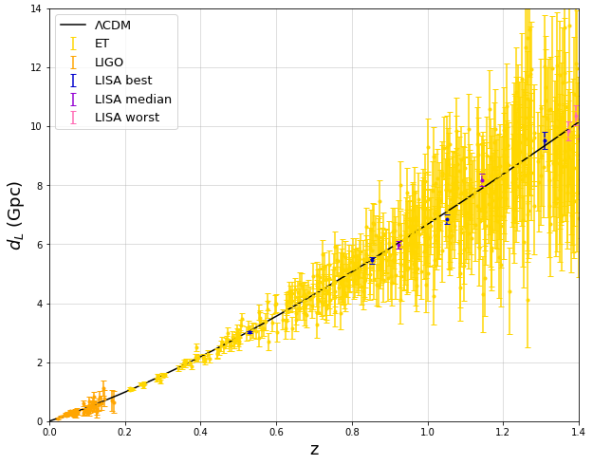

Figure 4.7: This figure shows the LIGO-Virgo, 3 cases of LISA and ET catalogs Luminosity distance, in Gpc, as a function of redshift with redshift between 0 and 1.4. The ΛCDM model is plotted as a solid gray line.

when we present their correspond mock catalog in low redshift regime which is shown in fig. 4.7. We can see that the number of LIGO events is much larger than the number of ET events. They are limited within the range $z \in [0.025, 0.3]$, but the error bars enlarge when redshift increases. In addition, the first ET event with a much smaller error bar appears right after the furthest event of LIGO. This gives an insight why LIGO is unable to give a proper constraint alone. An

idea raised in [27] consists of considering of a joint analysis using the extreme low redshift LIGO events $z \in [0.025, 0.0625]$ to complement the other missions such as LISA. The following plot shows a joint analysis on LISA with LIGO data:

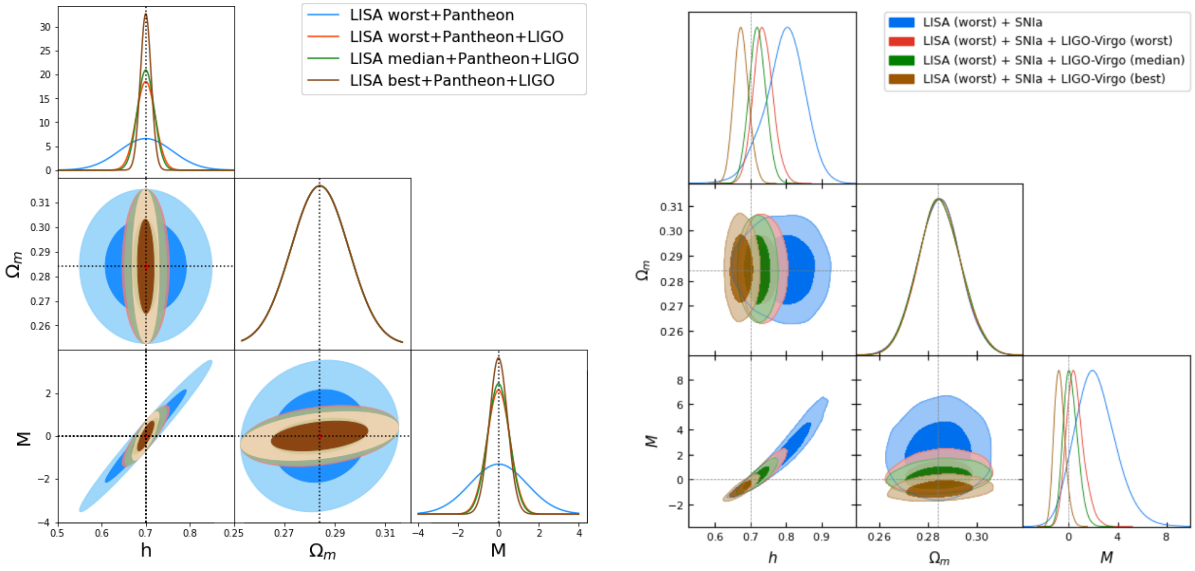

Figure 4.8: The left panel shows the parameter constraints computed by the FM method using the worst, median and best LISA catalogs joined analysis with LIGO-Virgo collaboration and Pantheon SnIa data. The worst LISA catalog with Pantheon is also shown for comparison. The right panel shows the parameter constraints computed by MCMC from [27]. Dotted lines represent the fiducial ΛCDM values.

Let us compare the left panel of both fig. 4.3 and fig. 4.8. There is a substantial improvement in the worst catalog with the complement of LIGO data, and a slight improvement on the median class, and both constraints are compatible. Meanwhile, the best LISA catalog shows almost no improvement.

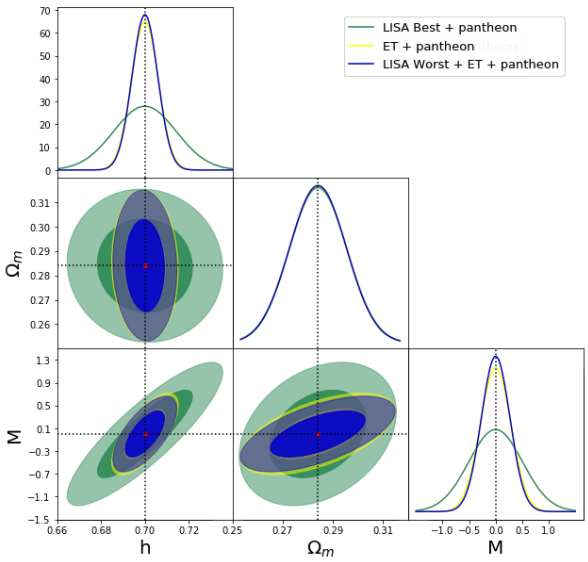

Figure 4.9: Parameter constraints computed by FM method using the worst, median and best LISA catalogs joined analysis with ET and Pantheon SnIa data. The worst LISA catalog+Pantheon and ET catalog+Pantheon are also shown for comparison. Dotted lines represent the fiducial ΛCDM values.

Lastly, we attempt to further increase the quality of our constraints, using the joint analysis of all missions. In fig. 4.9 show that the constraints in the case of LISA worst catalogs+ET+Pantheon data are extremely close to the case ET+Pantheon data, also the results computed by the best and median LISA catalogs are very close to the worst catalogs. For clarity, the best and median case are not shown in the figure. In conclusion, using ET + Pantheon data is already enough to give a tight parameter constraints. Likewise, LIGO-Virgo + ET showed no significant improvements, as expected given the high quality of the constraints provided by ET alone.

4.2 $n = 2$ model

In this section we derive the $E(z)$ function and the modification of the GW luminosity distance for the polynomial $f(Q)$ model with $n = 2$. We start from the modified first Friedmann equation presented in Eq. (2.36):

$$f_Q Q - \frac{1}{2} f = 8\pi G \rho \tag{4.12}$$

with, a function f in the form:

$$f = Q + \alpha Q^2 \,, \tag{4.13}$$

where α is a constant and Q is still $Q = 6H^2$.
Since the expected SSs events are expected to be observed in late time universe, we consider it to be composed only of ordinary matter, dark matter and a cosmological constant and neglect radiation.
The $E(z)$ function for $n = 2$ model in late time universe regime:

$$E^2 + \frac{3}{2} M^* E^4 = \Omega_m^0 (1+z)^3 + \Omega_\Lambda^0 \tag{4.14}$$

where $M^* = \frac{6^2\alpha H_0^2}{3}$ is the redefined free parameter, and $\Omega_\Lambda^0 = \frac{3}{2}M^* + 1 - \Omega_m^0$ to satisfy the condition $E(z=0) = 1$.
The explicit $E^2(z)$ function is:

$$E^2 = \frac{-1 + \sqrt{-3M^*(-2\Omega_m^0 z^3 - 6\Omega_m^0 z^2 - 6\Omega_m^0 z - 3M^* - 2) + 1}}{3M^*} \tag{4.15}$$

The GW luminosity distance is:

$$d_L^{(GW)}(z, \Omega_m^0, M^*, h) = \sqrt{\frac{1+M^*}{1+M^*E(z,\Omega_m^0,M^*,h)^2}}\, d_L(z, \Omega_m^0, M^*, h) \tag{4.16}$$

where $E(z) \equiv H(z)/H_0$.

4.2.1 Forecasts using Standard Sirens with $n = 2$

By looking at the expression for the luminosity distance of gravitational waves eq. (4.16), we can see that this model features a degeneracy between two of its parameters, M^* and Ω_m. To tackle this problem, we make use of the Pantheon sample with the marginalized SnIa likelihood developed in section 3.1.1, to fix both Ω_m and M^*. Figure 4.10 represent the 1σ and 2σ regions computed using the grid method. The results show that the 1σ value of Ω_m is 0.0249 and the 1σ value for M^* is 0.0243. The row and column components in the Fisher Matrix are constructed in the order (Ω_m, M^*, h). The 1σ values are added to 00-component in the Fisher Matrix and 11-component in the form $\frac{1}{\sigma^2_{\Omega_M}}$ and $\frac{1}{\sigma^2_{M^*}}$ respectively. Also we perform marginalization along M^* and Ω_m respectively, the value of each parameters with maximum likelihood are set at the fiducial value which located at $\Omega_m = 0.297$ and $M^* = 0$ when $n = 2$.

Now, we start the forecasts using the same mock catalogs of the three observatories generated in the previous section. Once again all the following 2D parameter constraints are marginalized along the third parameter.

LIGO-Virgo, LISA, ET Forecasts

Figure 4.11 shows the parameter constraints of LIGO-Virgo, worst, median, best case of LISA, and ET without the help by Pantheon date. We can see that only ET is able to provided a relative smaller region.

Therefore, in order to improve the constraints, we can perform a joint analysis either using the Pantheon data or the LIGO-Virgo SS catalog with the other two observatories.

As we compare fig. 4.11 and the left panel of fig. 4.12, with the help of LIGO-Virgo alone, the constraints of the 3-LISA cases become smaller on all three parameters, but there is no improvement on ET as it happened in chapter 6. On the right panel of fig. 4.12, we can see that with the help of Pantheon data, the 1σ and 2σ region become much smaller in LIGO-Virgo, LISA, and ET. The Pantheon data outperform LIGO-Virgo SS catalog.

For the joint analysis of LIGO-Virgo and Pantheon data, the constraints improve substantially, unlike in $n = \frac{1}{2}$ model, in which both LIGO-Virgo alone or LIGO-Virgo+Pantheon data do not provide useful constraints. For ET with Pantheon data, there are a relativity smaller improvement compare the other two observatories. For LISA mission without Pantheon data, the

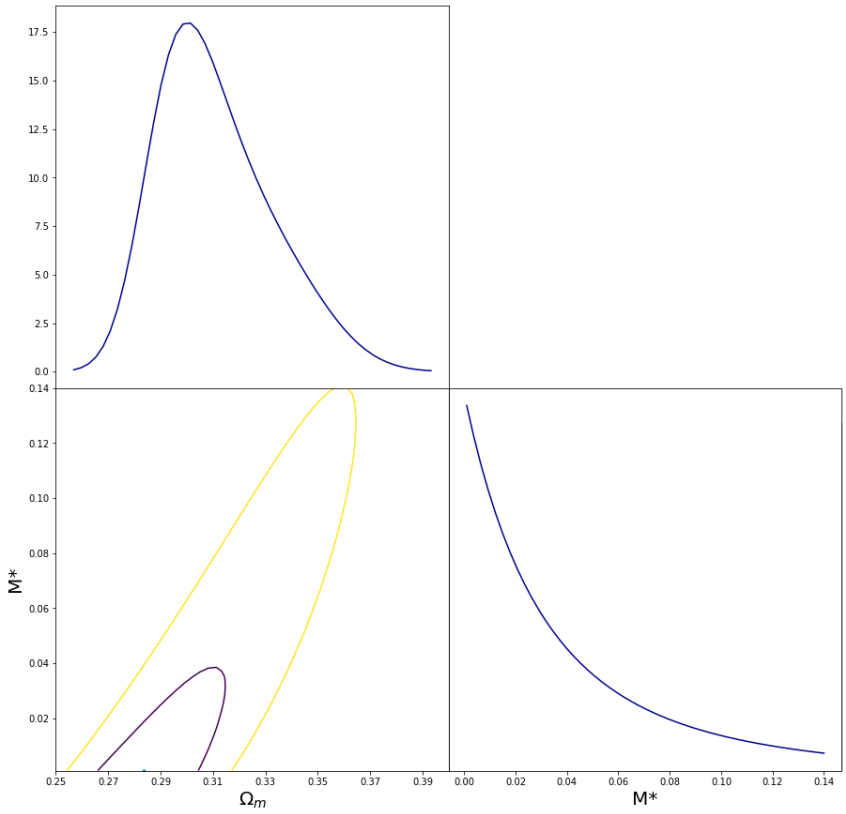

Figure 4.10: Bottom left figure refer to 1σ and 2σ region of M^* vs Ω_m computed by using the grid method, top figure refer to the likelihood summed along M^*, the bottom right figure refers to the likelihood summed along Ω_m

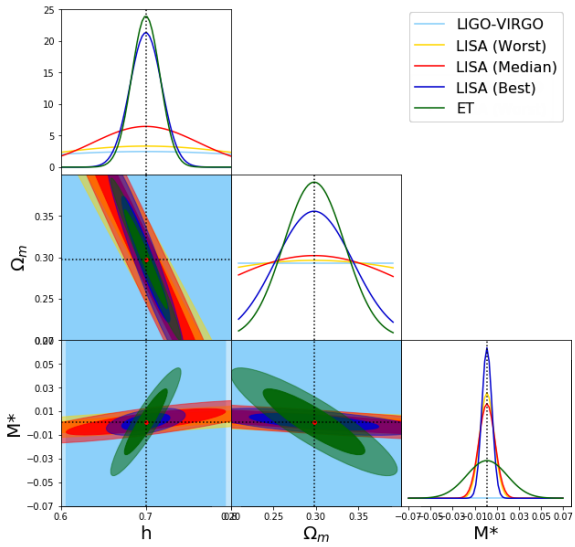

Figure 4.11: Parameter constraints computed by FM method using LIGO-Virgo, ET, worst, median and best LISA SS catalogs. The marginalized Likelihood for each parameter is shown in the diagonal plots. Dotted lines represent the fiducial values

regions of the best case are significantly smaller than the median and worst case, and the latter two are very close. However, with the help of Pantheon data, the three cases are very close with tight constraints. Let us further zoom in the plots LISA(3 case)+Pantheon and ET+Pantheon.

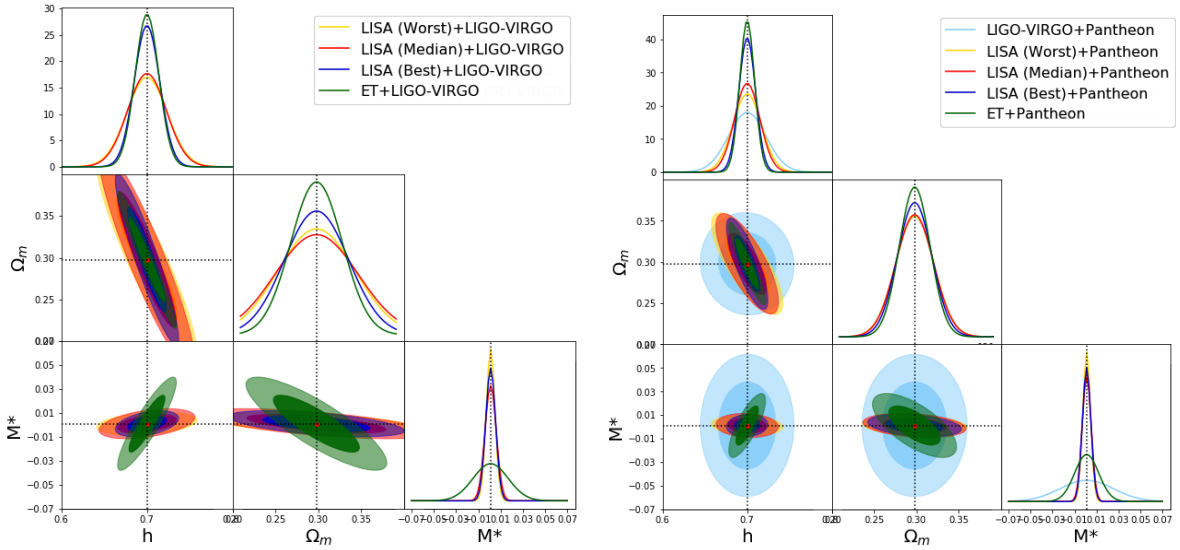

Figure 4.12: The left panel shows the parameter constraints of the joint analysis (LISA 3 case + LIGO-Virgo) and (ET + LIGO-Virgo) SS catalogs. The right panel shows the parameter constraints by joint analysis (LISA 3 case + Pantheon) and (ET + Pantheon). Both computed by FM method. The marginalized Likelihood for each parameters shown in the diagonal plots. Dotted lines represent the fiducial ΛCDM values.

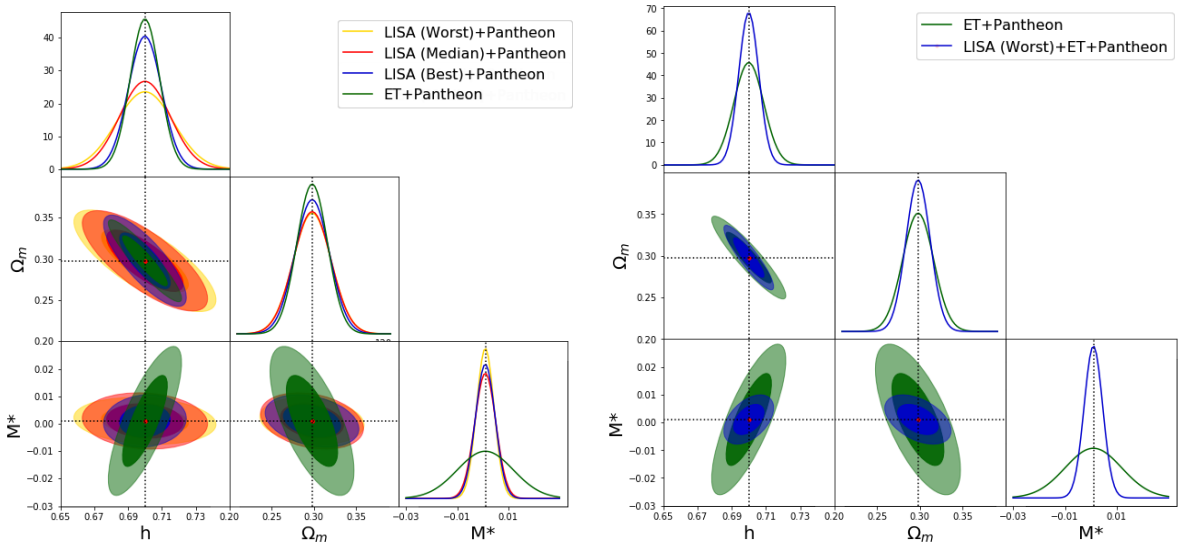

Figure 4.13: The left panel shows a zoom in Figure of 4.12 (right panel). The right panel shows the parameter constraints by joint analysis of LISA best, median and worst catalog with ET+ Pantheon SnIa data. Both computed by FM method. The marginalized Likelihood for each parameters shown in the diagonal plots. Dotted lines represent the fiducial ΛCDM values.

On the left figure of 4.13, we see that the best case give a slightly smaller region and the region of median and worst case are almost the same. Importantly, unlike $n = \frac{1}{2}$ model in which ET's constraint provide the best performance in all three parameters presented in fig. 4.6, LISA 3 classes of catalogs perform better constraint on parameter M^*. Therefore, it is interesting to combine LISA data with ET data to give us the best constraint on all the parameters. On

the right panel of fig. 4.13, we shows the 1σ, 2σ region of LISA(worst)+ET+Pantheon and ET+Pantheon, the former case provides a very tight constraints, and the constraints computed using the LISA's median catalog and the best catalogs are almost the same as the worst catalog, which are not shown in the plots for clarity. Therefore, we conclude that in practice LISA(worst)+ET+Pantheon data is already able to give a very good constraints on the three parameters, when we obtain the real data.

Chapter 5

Constraints on Quintessence models

In this chapter, we will demonstrate the Derivative Approximation for Likelihoods (DALI) method for reconstructing and forecasting posteriors. DALI extends the Fisher Matrix formalism by introducing also the higher order terms which allows for a much wider range of posterior shapes (non-Gaussian) while maintaining high computational speeds. We chose for the sake of example a Quintessence model and a Coupled Quintessence model [55, 56] as they provide both elliptical and non-elliptical confidence levels as can be shown by using, for example, the grid method. To demonstrate the validation of the Fisher Matrix method and DALI method in recovering the proper constraints, we compare the results with those computed by the grid method. Furthermore, the computational speed of the results computed by DALI method is 20 times larger than the grid method with grid size 50×50 in both models. In a Quintessence model, dark energy is governed by a dynamical scalar field. In coupled Quintessence model, the scalar field interacts with dark matter. In either of this the luminosity distance for gravitational waves is the same as the standard luminosity distance $d_L^{(GW)} = d_L$.
For the Quintessence model the luminosity distance is a function of several parameters:

$$d_L = d_L(\Omega_M, \Omega_\Lambda, \lambda) \tag{5.1}$$

which includes a constant parameter λ defining the evolution of the field such that $\phi = \phi_0 + \lambda N$. The corresponding $E(z)$ function is [55, 57]:

$$E^2(z) = \Omega_M \left[\frac{3}{3-\lambda^2}(1+z)^3 + \left(\frac{1-\Omega_M}{\Omega_M} + \frac{\lambda^2}{\lambda^2 - 3} \right) (1+z)^{\lambda^2} \right] \tag{5.2}$$

For the Coupled Quintessence model the Luminosity distance is a function with parameters:

$$d_L = d_L(\Omega_M, \Omega_\Lambda, \lambda, \beta) \tag{5.3}$$

where β is the coupling constant defining the interaction between the dark sectors.
The corresponding $E(z)$ function is [56, 57]:

$$E^2(z) = \frac{3(1+z)^{3-\gamma}}{3-\lambda^2-\gamma}\Omega_M + \left(1 - \Omega_M + \frac{\lambda^2+\gamma}{\lambda^2-3+\gamma}\Omega_M \right) (1+z)^{\lambda^2} \tag{5.4}$$

where $\gamma = \beta\lambda$.

5.1 The DALI method

In section 3.2.3, we know that the Fisher Matrix Method is a Taylor expansion of the χ^2 function up to the second order. The DALI method extends the formulation including third order and higher, in which the non-Gaussianities are taken into account. For the parameter constraint computation in DALI method, we follow Eq.(15) in Ref. [58]: P the posterior distribution refers to eq. (3.21) and the χ^2 that consist of the higher order terms is:

$$\chi^2 = F_{\alpha\beta}\Delta p_\alpha \Delta p_\beta + \left(S_{\alpha\beta\gamma}\Delta p_\alpha \Delta p_\beta \Delta p_\gamma + \frac{1}{4} Q_{\alpha\beta\gamma\delta}\Delta p_\alpha \Delta p_\beta \Delta p_\gamma \Delta p_\delta \right) \tag{5.5}$$

where we have the Fisher tensor:

$$F_{\alpha\beta} = \boldsymbol{\mu}_{,\alpha}\, M \boldsymbol{\mu}_{,\beta} \tag{5.6}$$

the Flexion tensor:

$$S_{\alpha\beta\gamma} = \boldsymbol{\mu}_{,\alpha\beta}\, M \boldsymbol{\mu}_{,\gamma} \tag{5.7}$$

and the Quarxion tensor:

$$Q_{\alpha\beta\gamma\delta} = \boldsymbol{\mu}_{,\delta\gamma}\, M \boldsymbol{\mu}_{,\beta\alpha} + O(3) \tag{5.8}$$

where $\Delta p_\alpha = p_\alpha - p_{\alpha(fid)}$, p_α denoted the fiducial value of the α^{th} parameter. The bold $\boldsymbol{\mu}$ is the theoretical model compared to a data set, which is the model vector, coma followed by α denotes partial derivative along the parameter p_α, the M is the data inverse covariance matrix and supposed our observations are uncorrelated, M is written as:

$$M = \mathrm{diag}(\sigma_1^2, ..., \sigma_B^2) \tag{5.9}$$

For the model vector $\boldsymbol{\mu}$ in our case, the model refer to the GW luminosity distance as a function of redshift, therefore:

$$\boldsymbol{\mu}_{,\alpha} = \frac{\partial d_{GW}^{(th)}(\boldsymbol{z})}{\partial p_\alpha} \tag{5.10}$$

and similarly for $\boldsymbol{\mu}_{,\alpha\beta}$.

An important advantage of the DALI method is its ability to reduce the flexion tensor from third-order to a combination of first-order and second-order derivatives with respect to the parameters. Additionally, it achieves the reduction of the Quarxion tensor from a fourth-order derivative to a combination of two second-order derivatives.

There are some similarities and differences in the properties of the Fisher Matrix Method and DALI method. Here we enumerate four major properties of the Fisher Matrix, where only the last two are shared with the DALI method:

- i) Fisher Matrix allows the evaluation of the n-σ confidence-level contours (only ellipses) analytically;
- ii) It allows performing marginalization over parameters simply by dropping rows and columns of the corresponding parameters from its inverse Fisher Matrix;
- iii) Fixing parameters at their best fit values is simply done by dropping the corresponding columns and rows of the corresponding parameters from the Fisher Matrix;

- iv) The FM of the product of two posteriors is the sum of the two posteriors FMs;

In the vast majority of cases, we are interested in one or two-dimensional contour plots of the posterior marginalized in all other parameters. Therefore, marginalization in the DALI method must be carried out numerically for the whole n-dimensional space.

5.2 Procedure of the parameter constraints computation

- Generate random redshift z_* values following the probability distribution function of standard sirens events and the number of values is matched to the expected observed number of events for the corresponding observatory, in this case ET;
- Compute the theoretical luminosity distances $d_L(z_*)$ from the obtained redshifts based on the fiducial values following fig. 5.1 and fig. 5.2;
- Compute the corresponding errors $\Delta d_L(z_*)$ for the obtained redshifts using the $\sigma_{tot}(z_*)$ for the corresponding observatory, and consider as the 1σ region for the luminosity distances;
- Create functions of the first and second derivative of the GW luminosity distance along the required parameters, e.g. Ω_M and λ in the Quintessence model and Ω_M, λ, γ in the Coupled Quintessence model;
- In the case of two parameters, create a 2×2 matrix, F, to store the Fisher Matrix components computed by the first derivative of GW luminosity distance function; a $2\times2\times2$ matrix, S, to store the Flexion terms computed by the first and second derivatives of the GW luminosity distance; and a $2 \times 2 \times 2 \times 2$ matrix, Q, to store the Quarxion terms computed by the second derivatives of the GW luminosity distance contracted with the covariance matrix (computed in the third step) correspondingly. Finite difference approach is used for the derivatives;
- Create arrays with sizes and dimensions that match the parameter space and store the corresponding Δp values. Contract each set of Δp values with the Fisher tensor, Flexion tensor and Quarxion tensor and sum the resulting values to obtain the χ^2 value. Repeat this process until it runs through the whole parameter space.
- Find the minimum χ^2 value and the corresponding parameter indexes;
- Plot the 1-σ and 2-σ contour levels with the minimum χ^2 value;

We finish this section with a final note about the computation of the Fisher, Flexion, Quarxion tensors. The Fisher components are arranged in the order: $[\Omega_M, \lambda]$, meaning that the F_{00} component is the contraction of the covariance matrix M with two first derivatives of $d_L^{(GW)}$ along Ω_M presented in Eq. (5.6), and similarly to the other components. For the Flexion tensor presented in Eq. (5.7), a 3 dimension matrix S is created. The first and second index components correspond to the second derivative of $d_L^{(GW)}$ along the parameters and the third index corresponds to the first derivative. Therefore, considering the symmetry of second derivatives

(Schwarz's theorem), $S_{1,0,0} = S_{0,1,0}$ and $S_{1,0,1} = S_{0,1,1}$. Similarly to the 4 dimension Quarxion Matrix Q Eq. (5.8), the first two indexes correspond to the second derivative, the third and fourth indexes correspond to the other second derivative. This also implies the following symmetry in the Quarxion tensor $Q_{0,1,1,1} = Q_{1,1,0,1} = Q_{1,0,1,1} = Q_{1,1,1,0} = Q_{1,0,0,0} = Q_{0,0,0,1} = Q_{0,0,1,0} = Q_{0,1,0,0} = Q_{1,0,1,0} = Q_{1,0,0,1} = Q_{0,1,0,1} = Q_{0,1,1,0}$. We use these symmetries to speed up the computation of the χ^2 function.

5.3 Einstein Telescope forecasts in Quintessence model

For the Quintessence model, two sets of SS mock data are generated according to the fiducial values as described in the caption of fig. 5.1. Then we perform constraints on the Ω_M, λ parameter space for both cases. On the top row, the constraints are computed by the grid method, are highly non-Gaussian. Since the grid method uses the mock data, the contour regions and the likelihood maxima are slightly changed due to the different random realizations of the mock catalogs. We can also see that the DALI approximation (bottom) is very close to the one computed by the grid method in both cases, but the Fisher Matrix method (middle) is not able to provide the appropriate constraints.

5.4 Einstein Telescope forecasts in Coupled Quintessence model

Similarly, the Coupled Quintessence model, the plots in fig. 5.2 follow two sets of fiducial values as described in the caption, and we explored the λ, γ parameter spaces. The shape of the contour computed by the grid method (top) when $\lambda = 0.7$ is highly Gaussian, and both Fisher matrix method (middle) and DALI method (bottom) give a very good approximation. However, when the shape of the contour is highly non-Gaussian (for $\lambda = 0.1$), the Fisher matrix method is unable to give a proper constraint, but the DALI method performs very well.

We conclude that if the distribution is a Gaussian function, then the Fisher Matrix and the DALI methods give the same results. However, when the distribution is a non-Gaussian, the Fisher Matrix method on its own cannot tell us whether the distribution is Gaussian or not, but the DALI method provides a proper approximation. When we are dealing with a few parameters, the DALI method is a good choice due to the high computational speed, however, when the number of parameters is large, its implementation in a code becomes complex. It is advisable to use a MCMC method as an alternative.

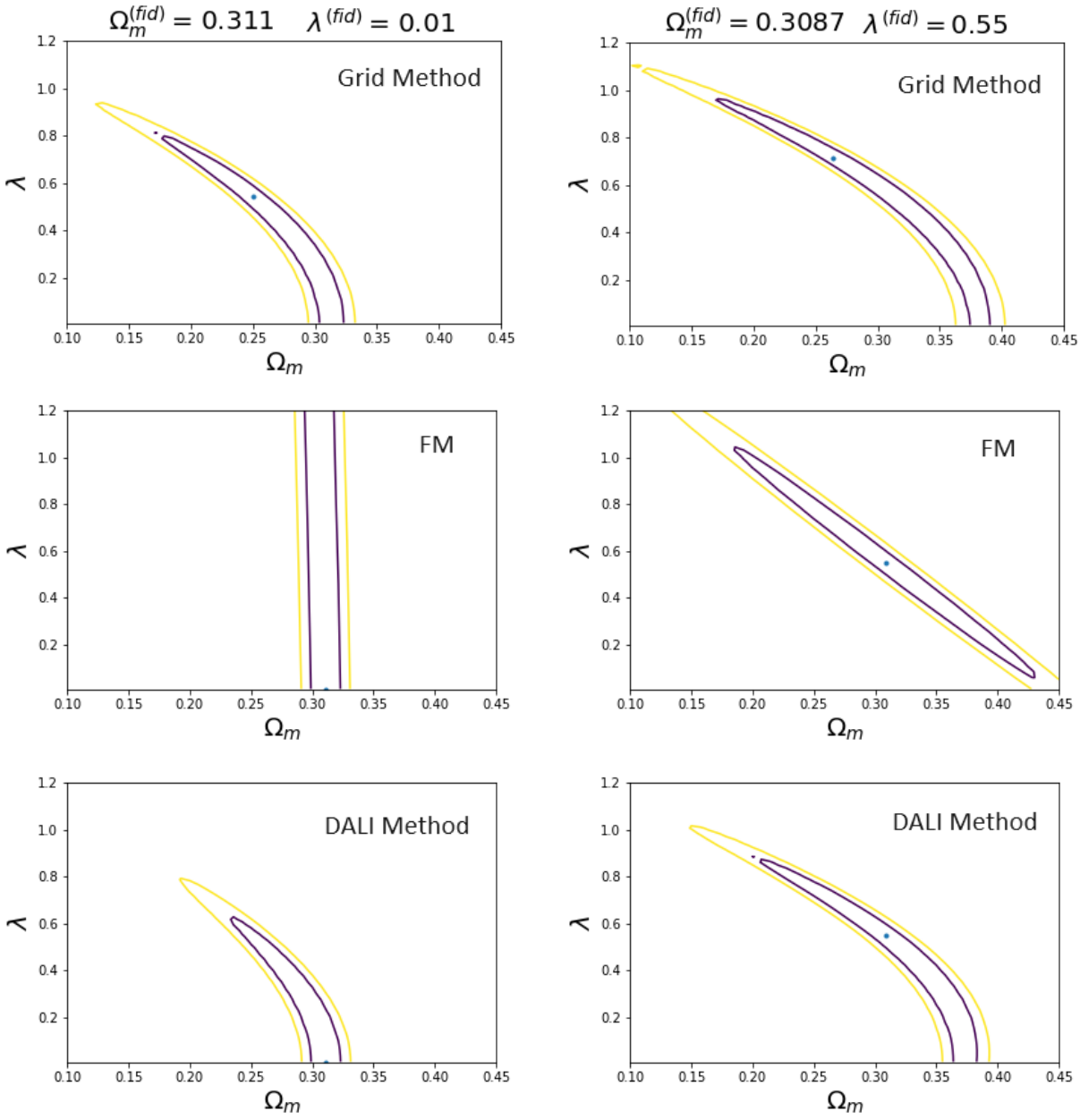

Figure 5.1: Contour plots made to obtain the most probable values for Ω_M and λ for the case of a Quintessence model with fiducial values $\Omega_M = 0.311$, $\lambda = 0.01$ on the left panel, and $\Omega_M = 0.3087$, $\lambda = 0.55$ for the right panel. The plots on the first row show the constraints computed using the grid method, the second row are computed using the Fisher Matrix method, the third row are computed using the DALI method.

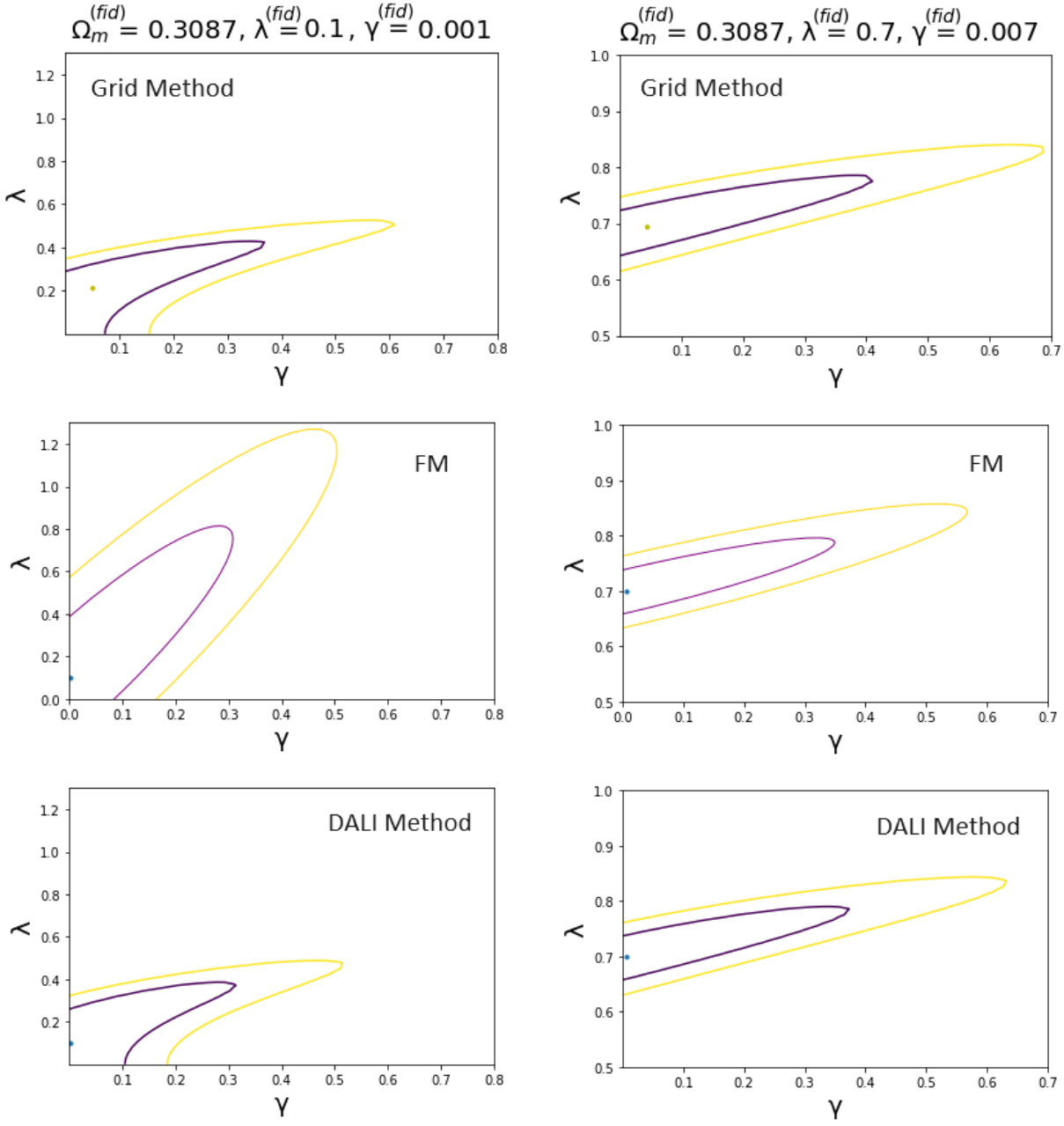

Figure 5.2: Contour plots made to obtain the most probable values for γ and λ for the case of a Coupled Quintessence model with fiducial $\Omega_M = 0.3087$, $\lambda = 0.1$, $\gamma = 0.001$ on the left panel, and $\Omega_M = 0.3087$, $\lambda = 0.7$, $\gamma = 0.007$ for the right panel. The plots on the first row show the constraints computed using the grid method, the second row are computed using the Fisher Matrix method, the third row are computed using the DALI method.

Chapter 6

Final Remarks

In this dissertation, we constructed Standard Siren mock catalogs based on a ΛCDM fiducial model for three observatories, one current observatory which is LIGO-Virgo collaboration and one future ground and one space based observatory. ET and LISA respectively. We have investigated a generic polynomial form $f(Q) = Q + \alpha Q^n$ which results in a cosmological model with one additional free parameter. First we chose $n = 1/2$, which results in a model with a ΛCDM background and then we explored the $n = 2$ case. Both cases lead to a modification on the luminosity distance of gravitational waves by an effective gravitational multiplicative term with respect to the standard luminosity distance.

For the first model, we have obtained using the Fisher matrix approach, consistent parameter constraints comparable to the ones computed using MCMC method [27], apart from the fact that the center of the ellipses are located on the fiducial values. This agreement can be explained by the highly elliptical likelihood function. Then we moved to the analysis for the three observatories. As a high number of events are expected to be observed by LIGO-Virgo and the Einstein Telescope, a single set of mock catalogs for each observatory was generated and proved to be able to give a representation of the "true" statistical distribution. We observed that due to the rapid increase in the error of the data points with redshift in the LIGO-Virgo observations, the data is unable to provide any constraint on the model by itself. We noticed, however, that given the good quality data in extreme low redshift events $z \in [0.025, 0.0625]$ which is not available for other observatories, LIGO-Virgo catalog can be used as a joint analysis with LISA and ET catalogs. This can be done by adding the Fisher Matrices for both missions to the LIGO-Virgo Fisher Matrix.

For LISA, we classify three sets of mock catalogs, the worst, median, and the best catalog based on how good the results on the parameter constraints are. The classification can be explained by the high number of low redshift events (below or equal to redshift 2) with small error bars that the best catalog has followed by the median and finally the worst case. Therefore the quality of the parameter constraints is dominated by the low redshift events. With the joint mission analysis with Pantheon SnIa data, only the best LISA catalog is comparable to ET in which case ET provides relatively tighter constraints. Also, using the joint mission with both LIGO-Virgo and Pantheon data with LISA's three catalogs, we showed that only the worst case the constraints are sufficiently improved as shown in fig. 4.8. We also illustrated the best

case scenario using all of the data in fig. 4.9 and concluded that the joint analysis of ET with Pantheon is already enough to provide the best constraints for future constraints of this model. Once again, the conclusions corroborate the results obtained with MCMC method in [27]

For the second model, the priors found using Pantheon data give information on both Ω_M and M^* instead of just Ω_M. Comparing LISA three classes of catalogs and ET with the joint analysis with either LIGO-Virgo or Pantheon data presented in fig. 4.12, we concluded that the improvement using Pantheon data outperforms the LIGO-Virgo constraints. We also compared the parameter constraints between LISA and ET with the complement of Pantheon data. We noticed that unlike the $n = 1/2$ model, in which the constraints for all parameter in ET mission are outperformed than LISA presented in fig. 4.6, all 3 LISA catalogs provided better constraint on parameter M^* in the $n = 2$ model. This brought us to perform a joint analysis between LISA and ET with the assistance of Pantheon data presented in fig. 4.13. The results show that the constraints are tight and very similar between the three classes of LISA catalogs in combination with ET and Pantheon data. Therefore, we concluded that in future observations, even if LISA provided us the worst case observations, by jointing both ET and Pantheon data, we have much higher certainty on the verification of $n = 2$ model.

In the final part of this dissertation, we explored the DALI method by computing the parameter constraints when introducing higher order terms in the Fisher Matrix. A quintessence model and a Coupled Quintessence model were used as they show highly non-Gaussian 1σ, 2σ contour levels when computed by the grid method. These correction terms in the DALI method can provide a proper approximation to the highly non-Gaussian likelihood in the cases when the Fisher Matrix method fails. Also, the higher computational speed compared to the MCMC and grid methods make it a compelling alternative. In our case, the results show that the DALI method is at least 20 times faster than the grid method with grid size 50×50 in both models. For simplification, we fixed the Ω_M value at the maximum likelihood and explored the constraints in the parameter space $\gamma - \lambda$. We leave the case of performing marginalization for future work as this is more delicate, e.g., when a three-dimensional parameter space has to be considered, meaning the Flexion and Quarxion tensor components increase substantially.

6.1 Future Work

There are a number of tasks worth investigation beyond the present work:

- Perform dynamical system analysis on both $f(Q)$ models to determine the regions in parameter space leading to viable cosmologies.
- Perform marginalization using DALI method on the Coupled Quintessence models;
- A study on PyCBC python package used as the gravitational wave strain generation for varying parameters like the masses, the spins of the binary system. These data sets can be used to train a AI machine learning algorithm to output the parameter constraints on a given model. It would be very interesting if we apply the Fisher Matrix/DALI method as an alternative.

Bibliography

[1] Albert Einstein. «Zur Allgemeinen Relativitätstheorie». In: *Sitzungsber. Preuss. Akad. Wiss. Berlin (Math. Phys.)* (1915), pp. 778–786.

[2] Edwin Hubble. «A relation between distance and radial velocity among extra-galactic nebulae». In: *Proc. Nat. Acad. Sci.* 15 (1929), pp. 168–173. DOI: 10.1073/pnas.15.3.168.

[3] Adam G. Riess et al. «Observational Evidence from Supernovae for an Accelerating Universe and a Cosmological Constant». In: *The Astronomical Journal* 116.3 (Sept. 1998), pp. 1009–1038. DOI: 10.1086/300499. URL: https://doi.org/10.1086%2F300499.

[4] F. Zwicky. «Die Rotverschiebung von extragalaktischen Nebeln». In: *Helvetica Physica Acta* 6 (Jan. 1933), pp. 110–127.

[5] A. A. Penzias and R. W. Wilson. «A Measurement of Excess Antenna Temperature at 4080 Mc/s.» In: 142 (July 1965), pp. 419–421. DOI: 10.1086/148307.

[6] R. H. Dicke et al. «Cosmic Black-Body Radiation». In: *Astrophys. J.* 142 (1965), pp. 414–419. DOI: 10.1086/148306.

[7] George F. Smoot et al. «Structure in the COBE differential microwave radiometer first year maps». In: *Astrophys. J. Lett.* 396 (1992), pp. L1–L5. DOI: 10.1086/186504.

[8] C. L. Bennett et al. «The Microwave Anisotropy Probe (MAP) mission». In: *Astrophys. J.* 583 (2003), pp. 1–23. DOI: 10.1086/345346. arXiv: astro-ph/0301158.

[9] The Planck Collaboration. *The Scientific Programme of Planck*. 2006. arXiv: astro-ph/0604069 [astro-ph].

[10] Matthew Colless et al. «The 2dF Galaxy Redshift Survey: Spectra and redshifts». In: *Mon. Not. Roy. Astron. Soc.* 328 (2001), p. 1039. DOI: 10.1046/j.1365-8711.2001.04902.x. arXiv: astro-ph/0106498.

[11] Bruce Margony. «The Sloan Digital Sky Survey». In: *Philosophical Transactions of the Royal Society of London. Series A: Mathematical, Physical and Engineering Sciences* 357.1750 (Jan. 1999). Ed. by G. P. Efstathiou et al., pp. 93–103. DOI: 10.1098/rsta.1999.0316. URL: https://doi.org/10.1098%2Frsta.1999.0316.

[12] and R. Scaramella et al. «iEuclid/i preparation». In: *Astronomy &amp Astrophysics* 662 (June 2022), A112. DOI: 10.1051/0004-6361/202141938. URL: https://doi.org/10.1051%2F0004-6361%2F202141938.

[13] Sean M. Carroll. «The Cosmological constant». In: *Living Rev. Rel.* 4 (2001), p. 1. DOI: 10.12942/lrr-2001-1. arXiv: astro-ph/0004075.

[14] P. J. E. Peebles. «Large scale background temperature and mass fluctuations due to scale invariant primeval perturbations». In: *Astrophys. J. Lett.* 263 (1982). Ed. by M. A. Srednicki, pp. L1–L5. DOI: 10.1086/183911.

[15] Leandros Perivolaropoulos and Foteini Skara. «Challenges for ΛCDM: An update». In: (May 2021). arXiv: 2105.05208 [astro-ph.CO].

[16] Adam G. Riess. «The expansion of the Universe is faster than expected». In: *Nature Reviews Physics* 2.1 (Dec. 2019), pp. 10–12. DOI: 10.1038/s42254-019-0137-0. URL: https://doi.org/10.1038%2Fs42254-019-0137-0.

[17] E. Macaulay, I. K. Wehus, and H. K. Eriksen. «Lower Growth Rate from Recent Redshift Space Distortion Measurements than Expected from Planck». In: *Physical Review Letters* 111.16 (Oct. 2013). DOI: 10.1103/physrevlett.111.161301. URL: https://doi.org/10.1103%2Fphysrevlett.111.161301.

[18] Dominik J Schwarz et al. «CMB anomalies after Planck». In: *Classical and Quantum Gravity* 33.18 (Aug. 2016), p. 184001. DOI: 10.1088/0264-9381/33/18/184001. URL: https://doi.org/10.1088%2F0264-9381%2F33%2F18%2F184001.

[19] Spyros Basilakos and Leandros Perivolaropoulos. «Testing gamma-ray bursts as standard candles». In: *Monthly Notices of the Royal Astronomical Society* 391.1 (Nov. 2008), pp. 411–419. DOI: 10.1111/j.1365-2966.2008.13894.x. URL: https://doi.org/10.1111%2Fj.1365-2966.2008.13894.x.

[20] D. M. Scolnic et al. *Pantheon analysis repository*. URL: https://github.com/dscolnic/Pantheon.

[21] R. A. Hulse and J. H. Taylor. «Discovery of a pulsar in a binary system». In: *Astrophys. J. Lett.* 195 (1975), pp. L51–L53. DOI: 10.1086/181708.

[22] B. P. Abbott et al. «Observation of Gravitational Waves from a Binary Black Hole Merger». In: *Phys. Rev. Lett.* 116 (6 2016), p. 061102. DOI: 10.1103/PhysRevLett.116.061102. URL: https://link.aps.org/doi/10.1103/PhysRevLett.116.061102.

[23] The LIGO Scientific Collaboration and The Virgo Collaboration. «GW170817: Observation of Gravitational Waves from a Binary Neutron Star Inspiral». In: *Phys. Rev. Lett. 119 161101 (2017)* (Oct. 2017). DOI: 10.1103/PhysRevLett.119.161101. arXiv: 1710.05832 [gr-qc].

[24] The LIGO Scientific Collaboration and the Virgo Collaboration. «Properties and astrophysical implications of the 150 Msun binary black hole merger GW190521». In: *Astrophys. J. Lett. 900, L13 (2020)* (Sept. 2020). DOI: 10.3847/2041-8213/aba493. arXiv: 2009.01190 [astro-ph.HE].

[25] B. F. Schutz. «Determining the Hubble constant from gravitational wave observations». In: 323.6086 (Sept. 1986), pp. 310–311. DOI: 10.1038/323310a0.

[26] Daniel E. Holz, Scott A. Hughes, and Bernard F. Schutz. «Measuring cosmic distances with standard sirens». In: *Physics Today* 71.12 (Dec. 2018), pp. 34–40. ISSN: 0031-9228. DOI: 10.1063/PT.3.4090. eprint: https://pubs.aip.org/physicstoday/article-pdf/71/12/34/10120184/34_1_online.pdf. URL: https://doi.org/10.1063/PT.3.4090.

[27] José Ferreira et al. «Forecasting F(Q) cosmology with ΛCDM background using standard sirens». In: *Phys. Rev. D* 105.12 (2022), p. 123531. DOI: 10.1103/PhysRevD.105.123531. arXiv: 2203.13788 [astro-ph.CO].

[28] Ray Inverno. *Introducing Einstein's relativity*. Oxford England New York: Clarendon Press Oxford University Press, 1992. ISBN: 9780198596868.

[29] Jose Beltrán Jiménez, Lavinia Heisenberg, and Tomi S. Koivisto. «The Geometrical Trinity of Gravity». In: *Universe* 5.7 (2019), p. 173. DOI: 10.3390/universe5070173. arXiv: 1903.06830 [hep-th].

[30] Sebastian Bahamonde et al. «Teleparallel Gravity: From Theory to Cosmology». In: (June 2021). arXiv: 2106.13793 [gr-qc].

[31] Daniel Baumann. «Cosmology». In: *Part III Mathematical Tripos* (2012).

[32] Jose Beltran Jimenez, Lavinia Heisenberg, and Tomi Koivisto. «Coincident General Relativity». In: *Phys. Rev. D 98, 044048 (2018)* (Oct. 2017). DOI: 10.1103/PhysRevD.98.044048. arXiv: 1710.03116 [gr-qc].

[33] Jose Beltrán Jiménez et al. «Cosmology in $f(Q)$ geometry». In: *Phys. Rev. D 101, 103507 (2020)* (June 2019). DOI: 10.1103/PhysRevD.101.103507. arXiv: 1906.10027 [gr-qc].

[34] Michele Maggiore. *Gravitational Waves: Volume 1: Theory and Experiments Volume 1. Theory and Experiments*. Oxford University Press, USA, 2007, p. 288. ISBN: 9780198570745.

[35] Alessandra Buonanno. *Gravitational waves*. 2007. arXiv: 0709.4682 [gr-qc].

[36] Michele Maggiore. *Gravitational Waves : Volume 2 Astrophysics and Cosmology. Astrophysics and Cosmology*. Oxford University Press, 2018. ISBN: 9780198570899.

[37] Enis Belgacem et al. «The gravitational-wave luminosity distance in modified gravity theories». In: *Phys. Rev. D 97, 104066 (2018)* (Dec. 2017). DOI: 10.1103/PhysRevD.97.104066. arXiv: 1712.08108 [astro-ph.CO].

[38] Enis Belgacem et al. «Testing modified gravity at cosmological distances with LISA standard sirens». In: *Journal of Cosmology and Astroparticle Physics* 2019.07 (July 2019), pp. 024–024. DOI: 10.1088/1475-7516/2019/07/024. URL: https://doi.org/10.1088%2F1475-7516%2F2019%2F07%2F024.

[39] M. Goliath et al. «Supernovae and the nature of the dark energy». In: *Astronomy & Astrophysics* 380.1 (Dec. 2001), pp. 6–18. DOI: 10.1051/0004-6361:20011398. arXiv: astro-ph/0104009 [astro-ph].

[40] M. Goliath et al. «Supernovae and the nature of the dark energy». In: *Astronomy &amp Astrophysics* 380.1 (Dec. 2001), pp. 6–18. DOI: 10.1051/0004-6361:20011398. URL: https://doi.org/10.1051%2F0004-6361%3A20011398.

[41] Luca Amendola. *Dark energy. theory and observations*. Cambridge University Press, 2010. ISBN: 9780521516006.

[42] Andreas Albrecht et al. «Findings of the Joint Dark Energy Mission Figure of Merit Science Working Group». In: (Jan. 2009). arXiv: 0901.0721 [astro-ph.IM].

[43] Dan Coe. *Fisher Matrices and Confidence Ellipses: A Quick-Start Guide and Software*. 2009. arXiv: 0906.4123 [astro-ph.IM].

[44] The LIGO Scientific Collaboration. «Advanced LIGO». In: *Classical and Quantum Gravity* 32.7 (Mar. 2015), p. 074001. DOI: 10.1088/0264-9381/32/7/074001.

[45] The Virgo Collaboration. «Advanced Virgo: a second-generation interferometric gravitational wave detector». In: *Classical and Quantum Gravity* 32.2 (Dec. 2014), p. 024001. DOI: 10.1088/0264-9381/32/2/024001.

[46] Michele Maggiore et al. «Science case for the Einstein telescope». In: *Journal of Cosmology and Astroparticle Physics* 2020.03 (Mar. 2020), pp. 050–050. DOI: 10.1088/1475-7516/2020/03/050. arXiv: 1912.02622 [astro-ph.CO].

[47] Macarena Lagos et al. «Standard sirens with a running Planck mass». In: *Phys. Rev. D 99, 083504 (2019)* (Jan. 2019). DOI: 10.1103/PhysRevD.99.083504. arXiv: 1901.03321 [astro-ph.CO].

[48] Tessa Baker and Ian Harrison. «Constraining Scalar-Tensor Modified Gravity with Gravitational Waves and Large Scale Structure Surveys». In: *Journal of Cosmology and Astroparticle Physics* 2021.01 (2021), pp. 068–068. DOI: 10.1088/1475-7516/2021/01/068. arXiv: 2007.13791 [astro-ph.CO].

[49] Chiara Caprini and Nicola Tamanini. «Constraining early and interacting dark energy with gravitational wave standard sirens: the potential of the eLISA mission». In: *Journal of Cosmology and Astroparticle Physics* 2016.10 (Oct. 2016), pp. 006–006. DOI: 10.1088/1475-7516/2016/10/006. arXiv: 1607.08755 [astro-ph.CO].

[50] Pau Amaro-Seoane et al. «Laser Interferometer Space Antenna». In: (Feb. 2017). arXiv: 1702.00786 [astro-ph.IM].

[51] Lorenzo Speri et al. «Testing the quasar Hubble diagram with LISA standard sirens». In: *Physical Review D* 103.8 (Apr. 2021), p. 083526. DOI: 10.1103/physrevd.103.083526. arXiv: 2010.09049 [astro-ph.CO].

[52] Enis Belgacem et al. «Modified gravitational-wave propagation and standard sirens». In: *Physical Review D* 98.2 (July 2018), p. 023510. DOI: 10.1103/physrevd.98.023510. arXiv: 1805.08731 [gr-qc].

[53] José Pedro Mota Valente Ferreira. « Constraining f(Q) cosmology with standard sirenes». In: *Tese de mestrado em Física (Astrofísica e Cosmologia), Universidade de Lisboa, Faculdade de Ciências* (2023). URL: https://renates2.dgeec.mec.pt/ppsqdet.asp.

[54] Wompherdeiki Khyllep, Andronikos Paliathanasis, and Jibitesh Dutta. «Cosmological solutions and growth index of matter perturbations in $f(Q)$ gravity». In: *Phys. Rev. D 103, 103521 (2021)* (Mar. 2021). DOI: 10.1103/PhysRevD.103.103521. arXiv: 2103.08372 [gr-qc].

[55] N. J. Nunes and James E. Lidsey. «Reconstructing the dark energy equation of state with varying alpha». In: *Physical Review D* 69.12 (June 2004). DOI: 10.1103/physrevd.69.123511. URL: https://doi.org/10.1103%2Fphysrevd.69.123511.

[56] Vitor da Fonseca, Tiago Barreiro, and Nelson J. Nunes. «A simple parametrisation for coupled dark energy». In: *Physics of the Dark Universe* 35 (Mar. 2022), p. 100940. DOI: 10.1016/j.dark.2021.100940. URL: https://doi.org/10.1016%2Fj.dark.2021.100940.

[57] Vítor Manuel da Fonseca. «Testar os acoplamentos da energia escura». In: *Tese de mestrado em Física (Astrofísica e Cosmologia), Universidade de Lisboa, Faculdade de Ciências* (2020). URL: http://hdl.handle.net/10451/48014.

[58] Elena Sellentin, Miguel Quartin, and Luca Amendola. «Breaking the spell of Gaussianity: forecasting with higher order Fisher matrices». In: *Monthly Notices of the Royal Astronomical Society* 441.2 (May 2014), pp. 1831–1840. DOI: 10.1093/mnras/stu689. URL: https://doi.org/10.1093%2Fmnras%2Fstu689.